HHS Public Access

Author manuscript

Chemistry. Author manuscript; available in PMC 2021 January 16.

Published in final edited form as:

Chemistry. 2020 January 16; 26(4): 900–912. doi:10.1002/chem.201904434.

Structural Characterization of a Series of N5-Ligated Mn^{IV}-oxo Species

Allyssa A. Massie[a], **Melissa C. Denler**[a], **Reena Singh**[b], **Arup Sinha**[b,c], **Ebbe Nordlander**[b], **Timothy A. Jackson**[*,a]

[a]The University of Kansas, Department of Chemistry and Center for Environmentally Beneficial Catalysis, 1567 Irving Hill Road, Lawrence, KS 66045, USA

[b]Lund University, Chemical Physics, Department of Chemistry, Box 124, SE-221 00 Lund, Sweden

[c]Department of Chemistry, School of Advanced Science, Vellore Institute of Technology, Vellore - 632014 Tamil Nadu, India

Abstract

Analysis of extended X-ray absorption fine structure (EXAFS) data for the Mn^{IV}-oxo complexes $[Mn^{IV}(O)(^{DMM}N4py)]^{2+}$, $[Mn^{IV}(O)(2pyN2B)]^{2+}$, and $[Mn^{IV}(O)(2pyN2Q)]^{2+}$ (^{DMM}N4py = *N*,*N*-bis(4-methoxy-3,5-di methyl-2-pyridylm ethyl)-*N*-bis(2-pyridyl)methylamine; 2pyN2B = (*N*-bis(1-methyl-2-benzimidazolyl)methyl-*N*-(bis-2-pyridylmethyl)amine, and 2pyN2Q = *N*,*N*-bis(2-pyridyl)-*N*,*N*-bis(2-quinolylmethyl)methanamine) afforded Mn=O and Mn-N bond lengths. The Mn=O distances for $[Mn^{IV}(O)(^{DMM}N4py)]^{2+}$ and $[Mn^{IV}(O)(2pyN2B)]^{2+}$ are 1.72 and 1.70 Å, respectively. In contrast, the Mn=O distance for $[Mn^{IV}(O)(2pyN2Q)]^{2+}$ was significantly longer (1.76 Å). We attribute this long distance to sample heterogeneity, which is reasonable given the reduced stability of $[Mn^{IV}(O)(2pyN2Q)]^{2+}$. The Mn=O distances for $[Mn^{IV}(O)(^{DMM}N4py)]^{2+}$ and $[Mn^{IV}(O)(2pyN2B)]^{2+}$ could only be well-reproduced using DFT-derived models that included strong hydrogen-bonds between second-sphere solvent 2,2,2-trifluoroethanol molecules and the oxo ligand. These results suggest an important role for the 2,2,2-trifluoroethanol solvent in stabilizing Mn^{IV}-oxo adducts. The DFT methods were extended to investigate the structure of the putative $[Mn^{IV}(O)(N4py)]^{2+}\cdot(HOTf)_2$ adduct. These computations suggest that a Mn^{IV}-hydroxo species is most consistent with the available experimental data.

Graphical Abstract:

Extended X-ray absorption fine structure (EXAFS) experiments for a series of oxomanganese(IV) species revealed manganese-oxygen bond distances longer than that predicted by DFT calculations. Further DFT studies with explicit trifluroethanol solvent molecules indicated that hydrogen bonding from the solvent lengthens the Mn=O bond.

[*]To whom correspondence should be addressed: Timothy A. Jackson, Phone: (785) 864-3968, taj@ku.edu.

Supporting Information. Fits of XAS pre-edge features, EXAFS fitting parameters, TD-DFT-computed pre-edge properties, molecular structures and metric parameters for DFT-optimized models of Mn^{IV}-oxo and Mn^{IV}-hydroxo complexes, and Cartesian coordinates for all DFT-optimized models.

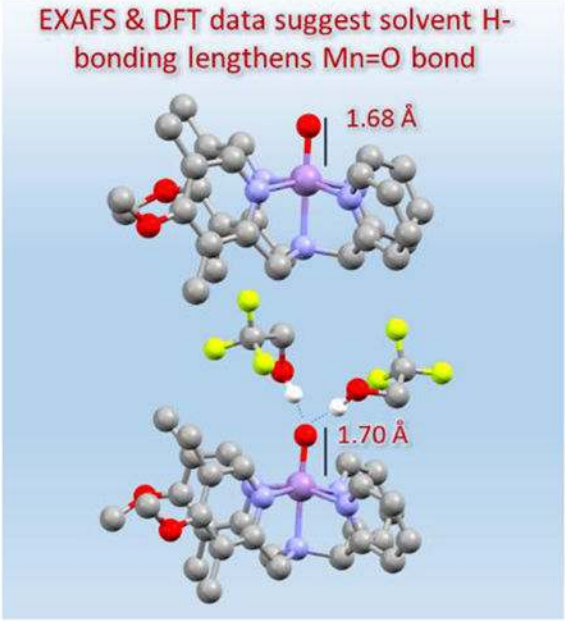

Keywords

Electronic structure; Oxido ligands; X-ray absorption spectroscopy

Introduction

High-valent metal-oxo species are often utilized in biological and synthetic oxidation reactions. These reactive centers are important for hydrogen atom transfer (HAT) reactions, which can serve as an initial step for the hydroxylation, halogenation, or desaturation of substrate C–H bonds.[1] In cytochrome P450 enzymes, Fe^{IV}-oxo porphyrin radical centers are proposed as a key intermediate in the functionalization of a wide range of C–H bonds.[2] Additionally, taurine/α-ketoglutarate dioxygenase (TauD) is proposed to utilize an Fe^{IV}-oxo center for the functionalization of the small molecule taurine.[1d, e, 3] The use of well-characterized Fe^{IV}-oxo model complexes has provided insight into the reactivity of these enzyme intermediates.[4] Importantly, these model systems have permitted detailed structural information for Fe^{IV}-oxo complexes supported by a variety of ligand types. Since the first crystal structure of an Fe^{IV}-oxo center was published in 2003,[5] there have been more than 60 other Fe^{IV}-oxo complexes reported in the literature featuring non-porphyrinic supporting ligands.[4] These species have been investigated spectroscopically and, in some cases, structurally, and extensive work has been done to understand their reactivity for a broad range of oxidation reactions.

In contrast, there is far less information concerning the structural properties of Mn^{IV}-oxo centers. To date, there is only a single example of an X-ray diffraction (XRD) structure for a mononuclear Mn^{IV}-oxo complex, $[Mn^{IV}(O)(ditox)_3]^-$ (where Hditox = ^{t}Bu$_2$MeCOH). [6] The Mn^{IV}-oxo coordination sphere in this complex consists of three alkoxide ligands, to give a distorted pseudo-tetrahedral geometry with approximate C_{3v} symmetry. Presumably

the all oxygen, trianionic ligand field stabilizes the Mn^{IV}-oxo unit. While this stabilization allowed for characterization by XRD, the strongly anionic ligand field also resulted in muted HAT reactivity.[6]

The most reactive Mn^{IV}-oxo centers reported to date feature neutral pentadentate ligands, and these complexes include $[Mn^{IV}(O)(N4py)]^{2+}$ and $[Mn^{IV}(O)(Bn\text{-}TPEN)]^{2+}$ (N4py = N,N-bis(2-pyridylmethyl)-N-bis(2-pyridyl)methylamine) and Bn-TPEN = N-benzyl-N,N′,N′-tris(2-pyridylmethyl)-1,2-diaminoethane)).[7] With the help of DFT calculations, the enhanced reactivity of these complexes was credited to a low-lying ligand-field excited state that offers a lower energy barrier for HAT than the ground state.[8] Inspired by this reactivity model, our groups introduced ligand perturbations to directly tune the energy of this excited state and determine any corresponding change in reactivity. These efforts led to the generation of the $[Mn^{IV}(O)(^{DMM}N4py)]^{2+}$, $[Mn^{IV}(O)(2pyN2B)]^{2+}$, and $[Mn^{IV}(O)(2pyN2Q)]^{2+}$ complexes (Figure 1), which showed a range of reaction rates with hydrocarbons.[9]

While this series of Mn^{IV}-oxo centers are all well-characterized spectroscopically, experimental insight into their structural properties is largely lacking. Although Mn K-edge X-ray absorption spectroscopy (XAS) has served as an extremely useful technique for characterization of Mn^{IV}-oxo centers, this method has been incompletely applied to several of these complexes.[7b, c, 10] MN K-edge XAS data for Mn^{IV}-oxo complexes of the N4py, ^{DMM}N4py, 2pyN2B, and 2pyN2Q ligands were previously reported.[9–10] For $[Mn^{IV}(O)(N4py)]^{2+}$, a thorough analysis of both the pre-edge and EXAFS regions was described.[7b, l0a] For the Mn^{IV}-oxo complexes of the ^{DMM}N4py, 2pyN2B, and 2pyN2Q ligands, however, the prior analysis only included the edge and pre-edge regions.Unfortunately, Mn^{IV}-oxo formation for this series is dependent on the use of 2,2,2-trifluoroethanol (TFE) as either a solvent or co-solvent. Halogenated solvents are nearly opaque to lower energy X-rays, and therefore interfere with the XAS measurements.[11] The solvent requirement for oxo formation could be attributed to the use of iodosobenzene (PhIO) as an oxidant for accessing the Mn^{IV}-oxo species, as PhIO exhibits limited solubility in most solvents and its dissolution requires the use of a protic solvent. However, another explanation could be that TFE provides a unique complex-solvent interaction that leads to stabilization of these Mn^{IV}-oxo adducts in solution.

In this present study, we describe the analysis of EXAFS data for Mn^{IV}-oxo complexes supported by the ^{DMM}N4py, 2pyN2B, and 2pyN2Q ligands in order to determine Mn-ligand metric parameters. These experimental metric parameters are in good agreement with those from DFT-derived models of the Mn^{IV}-oxo complexes that included second-sphere solvent (TFE) molecules. In each complex, these solvent molecules engage in strong hydrogen-bonding interactions with the oxo ligand, which leads to elongation of the Mn=O bond by ca. 0.02 Å. These results suggest that the protic TFE solvent molecules could play an important role in stabilizing this class of Mn^{IV}-oxo adducts. DFT calculations performed to investigate analogous hydrogen-bonding interactions for the Fe^{IV}-oxo complex $[Fe^{IV}(O)(N4py)]^{2+}$ showed weaker hydrogen bonding when compared to the $[Mn^{IV}(O)(N4py)]^{2+}$ complex. We also extended our DFT calculations to investigate the structure of the putative $[Mn^{IV}(O)(N4py)]^{2+}$-$(HOTf)_2$ adduct observed when $[Mn^{IV}(O)(N4py)]^{2+}$ is treated with

triflic acid.[12] Our computations suggest that, in this case, a Mn^{IV}-hydroxo species is most consistent with experimental observations.

Experimental and Computational Methods

Materials, Instrumentation, and Synthesis.

All chemicals and solvents were purchased from commercial vendors and were ACS reagent-grade quality or better. All chemicals were used as received, with the exception of MeCN and diethylether, which were sparged with argon and dried as described previously.[13] $Mn^{II}(OTf)_2{\cdot}2CH_3CN$, used for preparation of metal complexes, was synthesized according to a previously reported procedure.[14] Iodosobenzene was prepared from iodosobenzene diacetate following a published procedure without modification.[15] Ligands and corresponding Mn^{II} complexes were prepared as described previously.[9, 16] The formation of the Mn^{IV}-oxo species were monitored by electronic absorption spectroscopy using either a Varian Cary 50 Bio or an Agilent 8453 spectrophotometer. Both spectrophotometers were interfaced with Unisoku cryostats (USP-203-A), capable of maintaining temperatures of 25 °C.

Preparation of XAS Samples.

A 10 mM sample of $[Mn^{IV}(O)(^{DMM}N4py)]^{2+}$ was prepared by dissolving 12.5 mg (0.015 mmol) $[Mn^{II}(OTf)(^{DMM}N4py)](OTf)$ in 0.5 mL 2,2,2-trifluoroethanol (TFE), combining it with 6.6 mg (0.027 mmol) PhIO in 1 mL TFE and placing the reaction mixture into a 0.2 cm cuvette. The formation of $[Mn^{IV}(O)(^{DMM}N4py)]^{2+}$ was monitored by electronic absorption spectroscopy. At maximum formation, two XAS samples were prepared and flash frozen in liquid nitrogen.

A 10 mM XAS sample of $[Mn^{IV}(O)(2pyN2B)]^{2+}$ was prepared by dissolving 16.5 mg (0.020 mmol) $[Mn^{II}(OH_2)(2pyN2B)](OTf)^2$ in 2 mL of a TFE solution containing 44.0 mg (0.20 mmol) PhIO. The reaction mixture was placed into a 0.2 cm cuvette, where the formation of $[Mn^{IV}(O)(2pyN2B)]^{2+}$ was monitored by electronic absorption spectroscopy. At maximum formation, two XAS samples were prepared and flash frozen in liquid nitrogen.

A 10 mM sample of $[Mn^{IV}(O)(2pyN2Q)]^{2+}$ was prepared by dissolving 12.3 mg (0.015 mmol) $[Mn^{II}(OTf)(2pyN2Q)](OTf)$ in 0.5 mL TFE and 24.8 mg (0.11 mmol) PhIO in 1 mL TFE, which were mixed using a vortex mixer for 15 seconds. Two separate XAS samples were immediately prepared and flash frozen.

XAS Data Collection.

XAS data for all samples were collected at beamline 9-3 at the Stanford Synchrotron Radiation Lightsource (SSRL). Mn K-edge X-ray absorption spectra were collected over an energy range of 6.3 to 7.4 keV (Si(220) monochromator). The frozen samples were maintained at 10 K during data collection by an Oxford liquid He cryostat. XAS spectra were obtained as fluorescence excitation spectra using a Canberra 100-element Ge array detector. A reference spectrum of a manganese foil was collected for each scan and an

internal calibration was performed by setting the zero crossing of the second derivative of the K-edge energy of the reference spectra to 6539.0 keV. The high flux at beamline 9-3 led to photo-reduction of the Mn^{IV}-oxo samples. When multiple scans were collected on a single spot of the frozen sample, there was a noticeable shift of the edge to a lower energy. To reduce the effects of photoreduction, the beam was moved to different spots on the sample and only one scan was collected per spot. Four scans were collected for $[Mn^{IV}(O)(^{DMM}N4py)]^{2+}$, while nine scans with a smaller horizontal gap were collected for $[Mn^{IV}(O)(2pyN2Q)]^{2+}$. Nine scans were collected for $[Mn^{IV}(O)(2pyN2B)]^{2+}$.

XAS Data Analysis.

XAS data analysis was performed using the Demeter software package.[17] Individual scans of raw data were analyzed and combined using Athena, and extended X-ray absorption fine-structure (EXAFS) data were fit using Artemis. Phase and amplitude functions utilized in the fitting of the $k^3\chi(k)$ data were generated by *FEFF6*,[18] using density functional theory (DFT) optimized models (*vide infra*). For each fit, the parameters r, which describes the average scattering pathway distance, and σ^2 (Debye-Waller factor) were optimized individually for each path, and E_0 ($k = 0$ point) was a common variable for all paths. The parameter describing the degeneracy of the scattering atom, n, was fixed for each fit and systematically varied between fits in order to achieve better goodness of fit. The goodness of fit was evaluated using the R-factor (Equation 1).

$$R = \Sigma_{i=1}^{N} \left(\chi_i^{data} - \chi_i^{fit}\right)^2 / \Sigma_{i=1}^{N} \left(\chi_i^{data}\right)^2 \quad (1)$$

The typical error of analysis of EXAFS-fitted distances is ±0.02 Å.[19] Fits of the pre-edge areas were performed using the FityK software.[20] Pre-edge intensity was normalized relative to the tail of the fluorescence signal.

Electronic Structure Computations.

All computations were performed using the *ORCA* software package (versions 3.03 and 4.0.1.2).[21] DFT geometry optimizations employed the TPSS functional[22] with D3 corrections,[23] def2-TZVP (Mn, O, and N) and def2-SVP (C, F, and H) basis sets)[24] an SMD solvation model (for 2,2,2-trifluoroethanol))[25] and a dense integration grid (Grid6 in *ORCA*). Tight optimization and SCF criteria were invoked using the TightOpt and TightSCF keywords. The RI approximation, with def2-TZVP/J and def2-SVP/J auxiliary basis sets, was used for geometry optimizations. Structures of the Mn^{IV} complexes were converged to the 3/2 spin states. Pre-edge properties of the Mn^{IV}-oxo complexes were calculated using the TD-DFT method,[39] at a previously described level of theory,[10c] Electronic absorption spectra for Mn^{IV}-hydroxo complexes were calculated using both TD-DFT and CASSCF/NEVPT2 methods, using levels of theory described previously.[26] Frequency calculations for all Mn^{IV}-oxo species lacking second-sphere TFE molecules, and $[Mn^{IV}(O)(2pyN2Q)]^{2+}\cdot(TFE)_2$ showed no imaginary frequencies, ensuring that these structures represent true minima. The $[Mn^{IV}(O)(N4py)]^{2+}\cdot(TFE)_2$ and $[Mn^{IV}(O)(^{DMM}N4py)]^{2+}\cdot(TFE)_2$ structures each showed one small imaginary frequency (−7.30 and −25.18 cm^{-1}, respectively), associated with rotational modes of the methyl groups of TFE and the *para*-methoxy-pyridyl

moieties, respectively. Attempts to eliminate these imaginary modes through the use of a denser integration grid or tighter convergence criteria were unsuccessful. Cartesian coordinates for all DFT optimized models are included as Supporting Information (Tables S8 – S32).

Because hydrogen-bonding interactions can be quite sensitive to the choice of functional and/ or basis set,[27] we evaluated our conclusions regarding the structures of Mn^{IV}-oxo complexes with second-sphere TFE molecules by predicting geometries for $[Mn^{IV}(O)(2pyN2B)]^{2+}$ and $[Mn^{IV}(O)(2pyN2B)]^{2+}\cdot(TFE)_2$ using different functionals and basis sets. The results of this procedure, which are collected in the Supporting Information (Table S33), lead to several conclusions. First, and most importantly, in all systems considered the inclusion of the second-sphere TFE molecules leads to strong oxo-TFE hydrogen bonding interactions that cause an elongation of the Mn=O bond by ca. 0.02 Å. While the precise Mn=O bond lengths and O···H hydrogen-bonding distances vary depending on the level of theory employed, the ca. 0.02 Å elongation caused by hydrogen-bonding is observed. Second, for calculations using the TPSS functional, the lack of dispersion corrections *or* the use of a larger def2-TZPP basis set leads to longer Mn=O bonds. Specifically, for $[Mn^{IV}(O)(2pyN2B)]^{2+}$, Mn=O distances of 1.679 Å were calculated for both levels of theory, and for the $[Mn^{IV}(O)(2pyN2B)]^{2+}\cdot(TFE)_2$ complex with hydrogen-bonding, distances of 1.702 Å were calculated for both levels of theory. Third, the use of the M06-L functional, with either the large def2-TZVPP basis set or the ma-def2-SVP (for C and H) and ma-def2-TZVP (for Mn, O, and N) basis sets with diffuse functions, leads to results quite similar to the TPSS-D3 functional. Fourth, and finally, calculations employing the B3LYP-D3 functional gave somewhat shorter Mn=O distances and longer hydrogen-bonding distances, but the Mn=O bond elongation upon hydrogen-bonding was still observed. Thus, our conclusion that hydrogen-bonding with TFE molecules can lead to a Mn=O bond elongation appears to be fairly robust to the level of DFT theory employed.

Results and Analysis.

Mn K-edge XAS Edge and Pre-edge Properties for Mn^{IV}-oxo Complexes.

The Mn K-edge energies of the $[Mn^{IV}(O)(^{DMM}N4py)]^{2+}$, $[Mn^{IV}(O)(2pyN2B)]^{2+}$, $[Mn^{IV}(O)(N4py)]^{2+}$ and $[Mn^{IV}(O)(2pyN2Q)]^{2+}$ complexes fall within the narrow range of 6549.8 to 6550.8 eV (Table 1). The Mn K-edge of $[Mn^{IV}(O)(2pyN2Q)]^{2+}$ is ~0.5 eV lower than those of $[Mn^{IV}(O)(N4py)]^{2+}$, $[Mn^{IV}(O)(^{DMM}N4py)]^{2+}$ and $[Mn^{IV}(O)(2pyN2B)]^{2+}$ (Table 1). This difference can be appreciated in Figure 2, where the edge energy of $[Mn^{IV}(O)(2pyN2Q)]^{2+}$ is clearly lower than that of either $[Mn^{IV}(O)(^{DMM}N4py)]^{2+}$ or $[Mn^{IV}(O)(2pyN2B)]^{2+}$. Because the previously reported EPR spectra of $[Mn^{IV}(O)(2pyN2Q)]^{2+}$ shows a multiline signal due to the presence of some multi-nuclear species (potentially $Mn^{III}Mn^{IV}$ dimers), the lower edge energy of this complex is most likely due to the presence of this species.[9a] We note that the previously reported Mn K-edge energy for $[Mn^{IV}(O)(2pyN2Q)]^{2+}$, which was collected for a different sample, is 0.6 eV lower than that reported here (Table 1).[9a] This variation in edge energy based on sample preparation further supports our hypothesis that reduced sample homogeneity for $[Mn^{IV}(O)(2pyN2Q)]^{2+}$ can account for the lower edges of these samples.

Each of the Mn^{IV}-oxo complexes shows a prominent pre-edge feature centered at ca. 6542 eV (Figure 2). This feature contains contributions from Mn^{IV} 1s-to-3d transitions, which gain intensity through Mn^{IV} 3d-4p mixing induced by the short Mn=O distance.[10a] The pre-edge features of $[Mn^{IV}(O)(N4py)]^{2+}$, $[Mn^{IV}(O)(^{DMM}N4py)]^{2+}$, and $[Mn^{IV}(O)(2pyN2Q)]^{2+}$ were previously fit with only one pseudo-Voigt function centered near 6541.2 eV.[9a, 10a] However, higher resolution pre-edge data collected for $[Mn^{IV}(O)(^{DMM}N4py)]^{2+}$, $[Mn^{IV}(O)(2pyN2Q)]^{2+}$, and $[Mn^{IV}(O)(2pyN2B)]^{2+}$ at beamline 9-3 (SSRL) clearly reveal multiple pre-edge peak maxima (Figure 2, inset). For example, the pre-edge region for $[Mn^{IV}(O)(^{DMM}N4py)]^{2+}$ shows a prominent peak at 6541.6 eV, with shoulders at 6539.9 and 6543.2 eV (Figure S1). The pre-edge regions of $[Mn^{IV}(O)(2pyN2Q)]^{2+}$ and $[Mn^{IV}(O)(2pyN2B)]^{2+}$ are similar, although the latter sample appears to lack the shoulder at higher energy (Figure 2, inset).

The newly collected data were fit with two or three pseudo-Voigt functions (Figure S1), giving pre-edge areas similar to those reported previously (Table 1). The exception is the pre-edge area for $[Mn^{IV}(O)(2pyN2B)]^{2+}$, which is now 22.2, a dramatic increase compared to the previously reported value of 14.6.[9b] This increase in pre-edge area, along with the higher edge energy of the present sample (6550.2 versus 6549.6 eV), leads us to propose that the former sample was more heterogeneous, consisting of the Mn^{IV}-oxo center and secondary species.

The collective set of pre-edge areas determined from these present fits can be compared to values reported previously for $[Mn^{IV}(O)(N4py)]^{2+}$ and $[Mn^{IV}(O)(OH)(Me2EBC)]^{2+}$, although this comparison must be performed with some caution, as the pre-edge data were normalized differently.[10c] The pre-edge intensities for $[Mn^{IV}(O)(N4py)]^{2+}$ and $[Mn^{IV}(O)(OH)(Me2EBC)]^{2+}$ were normalized relative to the most intense fluorescence peak, whereas the tail of the EXAFS region was used to normalize data collected for $[Mn^{IV}(O)(^{DMM}N4py)]^{2+}$, $[Mn^{IV}(O)(2pyN2B)]^{2+}$, and $[Mn^{IV}(O)(2pyN2Q)]^{2+}$.[9a, 10a, c] To assess the effects of this different normalization process on the pre-edge area, we applied the latter normalization process to XAS data previously reported for $[Mn^{IV}(O)(N4py)]^{2+}$. Normalization to the tail of the EXAFS region resulted in a pre-edge area of 18.9, a significant increase compared to that determined when normalizing relative to the most intense fluorescence peak (12.7 units).[9a10c] Using the older normalization protocol, $[Mn^{IV}(O)(OH)(Me2EBC)]^{2+}$ had a pre-edge area higher than $[Mn^{IV}(O)(N4py)]^{2+}$ (14.2 versus 12.7). Therefore, if the pre-edge region for $[Mn^{IV}(O)(OH)(Me2EBC)]^{2+}$ were normalized to the EXAFS tail, it would likely have the highest pre-edge area for this series of Mn^{IV}-oxo complexes.

EXAFS Data and Analysis for Mn^{IV}-oxo Species.

The FT and raw EXAFS data for the $[Mn^{IV}(O)(^{DMM}N4py)]^{2+}$, $[Mn^{IV}(O)(2pyN2Q)]^{2+}$, and $[Mn^{IV}(O)(2pyN2B)]^{2+}$ complexes are shown in Figure 3, and best fits to date are collected in Table 2. More complete fitting information can be found in Tables S1 – S3. The FT spectrum of each Mn^{IV}-oxo complex is characterized by peaks at ca. 1.2, 1.6, and 1.9 Å that vary in intensity between the different complexes (Figure 3). Fits of the EXAFS data for $[Mn^{IV}(O)(^{DMM}N4py)]^{2+}$ and $[Mn^{IV}(O)(2pyN2B)]^{2+}$ reveal comparable metric parameters

(Table 2). In particular, the set of FT EXAFS features from 1.2 – 1.9 Å are well fit with an O shell ($n = 1$) near 1.70 Å and two N shells near 1.93 and 2.10 Å ($n = 2$ and 3, respectively). Additional FT peaks from ca. 2.1 – 2.5 Å can be fit considering two sets of C shells near 2.74 and 2.93 Å. The Mn–O scatterer distances for $[Mn^{IV}(O)(^{DMM}N4py)]^{2+}$ and $[Mn^{IV}(O)(2pyN2B)]^{2+}$, (1.72 and 1.70 Å, respectively) are in excellent agreement with Mn–O distances previously reported from EXAFS analyses of Mn^{IV}-oxo complexes in a pseudo-octahedral environment, which range from 1.58 to 1.71 Å.[7b, c, 10a, c, 28]

While the EXAFS analyses for $[Mn^{IV}(O)(^{DMM}N4py)]^{2+}$ and $[Mn^{IV}(O)(2pyN2B)]^{2+}$ yield metric parameters largely consistent with those of other Mn^{IV}-oxo complexes, the EXAFS fitting procedure for $[Mn^{IV}(O)(2pyN2Q)]^{2+}$ results in an O shell at the unrealistically long distance of 1.76 Å (Table 2). The Debye-Waller (σ^2) parameter for this shell is also unusually large for a single-atom shell at a short scattering distance. Given that $[Mn^{IV}(O)(2pyN2Q)]^{2+}$ has the fastest self-decay rate for this series of Mn^{IV}-oxo complexes, we attribute the unexpected EXAFS fits to the presence of secondary species. Prior EPR investigations of $[Mn^{IV}(O)(2pyN2Q)]^{2+}$ revealed the presence of signals characteristic of a $Mn^{III}Mn^{IV}$ dimer,[29] consistent with this proposal. Thus, we conclude that the fit for $[Mn^{IV}(O)(2pyN2Q)]^{2+}$ is not reflective of the true metric parameters of this complex.

Comparison of DFT and EXAFS Structures of Mn^{IV}-oxo Species.

DFT computations were previously used to predict structures for $[Mn^{IV}(O)(^{DMM}N4py)]^{2+}$ and $[Mn^{IV}(O)(2pyN2B)]^{2+}$.[9–10] These computations predicted Mn-oxo distances of 1.68 and 1.66 Å for $[Mn^{IV}(O)(^{DMM}N4py)]^{2+}$ and $[Mn^{IV}(O)(2pyN2B)]^{2+}$, respectively. In each case, these values are 0.04 Å shorter than those obtained from the EXAFS fits (1.72 and 1.70 Å; see Table 3). Although some variance between experimental and DFT-predicted metric parameters is expected, typically DFT methods are most reliable at predicting distances for strong, short metal-ligand bonds, such as the Mn-oxo bonds considered here.[30] It is possible that partial photoreduction of the Mn^{IV}-oxo XAS samples could account for a Mn=O distance longer than that expected based on the DFT computations. Alternatively, the DFT treatment, which considers the Mn^{IV}-oxo dications in a solvent continuum (*i.e.*, with no explicit interactions with solvent), could be incomplete.

Because a protic solvent, such as TFE, could be reasonably considered to have hydrogen-bonding interactions with the oxo ligands, we performed DFT geometry optimizations for models of $[Mn^{IV}(O)(N4py)]^{2+}$, $[Mn^{IV}(O)(^{DMM}N4py)]^{2+}$, and $[Mn^{IV}(O)(2pyN2B)]^{2+}$ that included two TFE molecules. These models were generated by placing the TFE molecules within hydrogen-bonding distance of the oxo ligands and then performing a DFT energy minimization with respect to all nuclear coordinates. For completeness, we also considered a structure of $[Mn^{IV}(O)(2pyN2Q)]^{2+}$ with explicit hydrogen-bonding interactions, although in this case we cannot compare the computational results to experimental distances. Our Mn^{IV}-oxo structures containing two TFE molecules are referred to as $[Mn^{IV}(O)(N4py)]^{2+}\cdot(TFE)_2$, $[Mn^{IV}(O)(^{DMM}N4py)]^{2+}\cdot(TFE)_2$, $[Mn^{IV}(O)(2pyN2Q)]^{2+}\cdot(TFE)_2$, and $[Mn^{IV}(O)(2pyN2B)]^{2+}\cdot(TFE)_2$. To provide a balanced comparison, we also re-optimized the structures of the Mn^{IV}-oxo complexes in the absence of added TFE using the same level of theory (our previous computational treatments lacked dispersion interactions, which we deemed

important to include here to properly model solvent-solute interactions).[9] The result of these computations are summarized in Tables 3 and 4, and molecular structures of the complexes with hydrogen-bonded TFE molecules are shown in Figure 4.

The structures of the Mn^{IV}-oxo complexes lacking the explicit TFE molecules are essentially identical to those previously reported.In each case, the Mn=O distance is near 1.68 Å (except for $[Mn^{IV}(O)(2pyN2B)]^{2+}$, which has a shorter Mn=O distance of 1.66 Å) and the Mn–Neq distances (which were obtained by averaging the equatorial Mn–N bond lengths) steadily increase from $[Mn^{IV}(O)(^{DMM}N4py)]^{2+}$ to $[Mn^{IV}(O)(N4py)]^{2+}$ to $[Mn^{IV}(O)(2pyN2Q)]^{2+}$ (Table 4). In the case of $[Mn^{IV}(O)(2pyN2B)]^{2+}$, the average equatorial Mn–N_{eq} distances for the structure lacking the TFE molecules is at 2.055 Å, which is the longest for this series. A previously determined structure of $[Mn^{IV}(O)(2pyN2B)]^{2+}$, which lacked dispersion corrections, predicted the average equatorial Mn–N_{eq} distance to be on the short end of the series. We speculate that the combination of dispersion corrections in the absence of explicit solvent interactions could lead to some errors in the DFT structure of $[Mn^{IV}(O)(2pyN2B)]^{2+}$. The DFT structure of $[Mn^{IV}(O)(2pyN2B)]^{2+}$ also gives the longest Mn–N_{amine} distane of 2.335 Å (Table 4). Notably, the XRD structure of the Fe^{IV}-oxo analogue, $[Fe^{IV}(O)(2pyN2B)]^{2+}$, also showed an Fe'$N_{amine}$ distance longer than those of $[Fe^{IV}(O)(N4py)]^{2+}$ and $[Fe^{IV}(O)(2pyN2Q)]^{2}$.[31] The axial elongation for the 2pyN2B-ligated complexes can be understood in part by the more obtuse methylene–C–N angles for the 5-membered ring of the benzimidazolyl arms when compared to their pyridyl and quinolinyl analogues (see Table S6). That C–C–N angle is approximately five degrees wider for the 2pyN2B ligand than for the other three ligands used in the present study (Table S6). As a consequence, the metal-Namine distance is elongated for the 2pyN2B ligand, in order not to cause strain in the five-membered ring that is formed by Mn–N_{amine}–CH_2–C–N_{eq}(donor) and to permit good orbital overlap between the benzimidazolyl N_δ atoms and the metal. The longer Mn–N_{amine} distance in $[Mn^{IV}(O)(2pyN2B)]^{2+}$ is directly reflected in a slightly shorter Mn=O distance that compensates for weaker donation from the axial N_{amine} function. A further structural manifestation of the more obtuse C–C–N angle is the larger displacement of the Mn^{IV} ion of $[Mn^{IV}(O)(2pyN2B)]^{2+}$ above the plane created by the four N_{eq} donors (Table S6). This out-of plane deviation is 0.15 Å for $[Mn^{IV}(O)(2pyN2B)]^{2+}$ and only 0.07 Å for the other Mn^{IV}-oxo complexes considered in this study.

Finally, we note that the oxo ligand in $[Mn^{IV}(O)(2pyN2Q)]^{2+}$ is shifted away from the quinoline groups, giving an O–Mn–N_{amine} angle of 170°. The other Mn^{IV}-oxo complexes show far more modest deviations in O–Mn–N_{amine} angle from 180° (Table 4). This tilting of the oxo ligand for the 2pyN2Q ligand was observed experimentally in the X-ray crystal structure of the $[Fe^{IV}(O)(2pyN2Q)]^{2+}$ complex.[31]

The optimized structures of the $[Mn^{IV}(O)(N4py)]^{2+}\cdot(TFE)_2$, $[Mn^{IV}(O)(^{DMM}N4py)]^{2+}\cdot(TFE)_2$, $[Mn^{IV}(O)(2pyN2Q)]^{2+}\cdot(TFE)_2$, and $[Mn^{IV}(O)(2pyN2B)]^{2+}\cdot(TFE)_2$ complexes each show two TFE groups with strong hydrogen-bonding interactions with the oxo ligand (Figure 4). The distances between the oxo ligand and the alcohol hydrogen atom of the TFE molecules varies from 1.622 – 1.749 Å, which indicates strong hydrogen-bonding interactions. For each Mn^{IV}-oxo complex, the strong oxo…$HOCH_2CF_3$ interaction causes an elongation in the Mn=O distance of ca. 0.02 Å (Table 4). For $[Mn^{IV}(O)(2pyN2B)]^{2+}\cdot$

$(TFE)_2$ and $[Mn^{IV}(O)(^{DMM}N4py)]^{2+}\cdot(TFE)_2$, this bond elongation leads to DFT-derived Mn=O bond lengths more consistent with those determined from fitting EXAFS data (Table 3),[10a]

The longest oxo…$HOCH_2CF_3$ distances come from the $[Mn^{IV}(O)(2pyN2Q)]^{2+}\cdot(TFE)_2$ and $[Mn^{IV}(O)(2pyN2B)]^{2+}\cdot(TFE)_2$ structures (Table 4). The steric bulk of the quinolinyl and benzimidazolyl groups prevent the TFE molecules from forming shorter hydrogen bonds with the oxo ligand, as illustrated in space-filling models of these Mn^{IV}-oxo adducts (Figure S3). The benzimidazolyl groups project C–H functions towards one of the TFE molecules and therefore have more restrictive steric properties for solvent interactions than the quinolinyl moieties (Figure S3). This effect, together with the bending of the Mn=O bond of $[Mn^{IV}(O)(2pyN2Q)]^{2+}$ away from the quinolinyl groups, can account for $[Mn^{IV}(O)(2pyN2B)]^{2+}\cdot(TFE)_2$ having the longest oxo…$HOCH_2CF_3$ distances (Table 4). The $[Mn^{IV}(O)(2pyN2B)]^{2+}\cdot(TFE)_2$ structure also shows a notable contraction in Mn–N_{eq} and Mn–N_{amine} distances compared to the structure lacking hydrogen bonding (Table 4). These changes are due to the Mn^{IV} ion shifting towards the equatorial plane created by the four Mn–N_{eq} donors (Table S6). The resulting metal-ligand distances for $[Mn^{IV}(O)(2pyN2B)]^{2+}\cdot(TFE)_2$ from the DFT computations are remarkably similar to those observed crystallographically for $[Fe^{IV}(O)(2pyN2B)]^{2+}$.[31] The crystal structure of that complex reveals one water molecule hydrogen bonded to the oxo ligand (with the water protons in calculated positions). We may thus compare the Mn-N_{amine} distance for $[Mn^{IV}(O)(2pyN2B)]^{2+}\cdot(TFE)_2$ (2.155 Å) with the analogous distance for $[Fe^{IV}(O)(2pyN2B)]^{2+}$, which is 2.115(6) Å.[31] The M–N_{eq} distances for $[Mn^{IV}(O)(2pyN2B)]^{2+}\cdot(TFE)_2$ and $[Fe^{IV}(O)(2pyN2B)]^{2+}$are also comparable – 1.999 vs 1.995 Å, respectively.[31]

Using the DFT-optimized models of the Mn^{IV}-oxo complexes, we also calculated pre-edge transitions using the TD-DFT method.[39] The TD-DFT-computed spectra of these complexes are quite similar (Figure S2 and Table S4),[32] each dominated by two transitions, at ca. 6542 and 6543 eV, corresponding to Mn^{IV} 1s → $3d_z^2$ one-electron excitations in the α- and β-spin manifolds. The inclusion of hydrogen-bonding interactions with TFE solvent molecules leads to a minor (ca. 15%) reduction in pre-edge intensity compared to the models lacking interactions with TFE. Even in the presence of explicit hydrogen-bonding interactions, the short Mn–O bond lengths cause significant Mn^{IV} $3d_z^2$-$4p_z$ mixing, which accounts for the high relative intensity of excitations to the Mn^{IV} $3d_z^2$ orbitals (Tables 5 and S4). The attenuation in pre-edge intensity observed for the Mn^{IV}-oxo complexes with hydrogen bonding is associated with a loss of 4p mixing into Mn^{IV} 3d manifold from 5.4% for $[Mn^{IV}(O)(N4py)]^{2+}$ to 3.9% for $[Mn^{IV}(O)(N4py)]^{2+}\cdot(TFE)_2$ (for this comparison we use the sum of Mn 4p (%) character in the acceptor MOs that contribute to the pre-edge region). The association between a loss in pre-edge intensity and an increase in the Mn-oxo bond length, as observed here, is consistent with a previous examination of manganese(IV) pre-edge properties.[33]

The DFT models including the TFE interactions give calculated pre-edge areas in excellent agreement with the experimental values (Table 5). The computations predict $[Mn^{IV}(O)(2pyN2B)]^{2+}$ to have the largest pre-edge area (24.7 units), in agreement with experiment (22.2 units). In addition, the energies of the TD-DFT transitions are within 0.5 eV of the

higher-energy bands observed in the experimental spectra (Table 5). Each TD-DFT-computed spectrum also contains a cluster of transitions near 6541 eV, which could account for the low-energy shoulder observed experimentally (Table 1). The good agreement between calculated and experimental pre-edge properties for these Mn^{IV} centers is consistent with previous TD-DFT investigations.[10c]

DFT Investigation of $[Fe^{IV}(O)(N4py)]^{2+}$ $(TFE)_2$ Species.

To determine if the hydrogen-bonding interactions postulated for the Mn^{IV}-oxo complexes could also be important for the structural properties of the analogous Fe^{IV}-oxo complexes,[31] we investigated hydrogen-bonding with TFE solvent for the latter complexes using DFT methods. The Fe^{IV}-oxo analogue of $[Mn^{IV}(O)(N4py)]^{2+}$, $[Fe^{IV}(O)(N4py)]^{2+}$ has been generated in both the protic solvent TFE and in the aprotic solvent MeCN. To investigate the effects of hydrogen-bonding with solvent for $[Fe^{IV}(O)(N4py)]^{2+}$, we developed DFT structures for $[Fe^{IV}(O)(N4py)]^{2+}$ and $[Fe^{IV}(O)(N4py)]^{2+}\cdot(TFE)_2$. These computations employ the same level of theory as that used for the Mn^{IV}-oxo computations (*vide supra*). The DFT-optimized structure of $[Fe^{IV}(O)(N4py)]^{2+}$ shows an Fe=O distance of 1.649 Å, with average $Fe–N_{equatorial}$ distances of 1.965 Å, and an $Fe–N_{amine}$ distance of 2.046 Å. These metric parameters are in good agreement with experimental distances from X-ray crystallography (Figure 5)[34] and with distances from previous DFT investigations.[35] In the DFT-optimized structure of $[Fe^{IV}(O)(N4py)]^{2+}\cdot(TFE)_2$, the two TFE molecules show strong hydrogen-bonding interactions with the oxo ligand (Figure 5). This interaction leads to a minor elongation in the Fe=O distance of 0.013 Å; minor changes are also observed in the Fe–N bond lengths (Figure 5). While the structure of $[Fe^{IV}(O)(N4py)]^{2+}\cdot(TFE)_2$ does contain oxo-TFE hydrogen-bonding interactions, these interactions are not as strong as those observed in the $[Mn^{IV}(O)(N4py)]^{2+}\cdot(TFE)_2$ structure. Specifically, the oxo---H distances in $[Fe^{IV}(O)(N4py)]^{2+}\cdot(TFE)_2$ are 0.1 Å longer than those in $[Mn^{IV}(O)(N4py)]^{2+}\cdot(TFE)_2$ (1.75 and 1.65 Å, respectively; see Figure 5 and Table 4). These results are consistent with previous observations that suggest that, at parity of coordination sphere, Mn^{IV}-oxo centers are more basic than their Fe^{IV}-oxo analogues.[36]

DFT Investigation of $[Mn^{IV}(O)(N4py)]^{2+}(HOTf)_2$ Species.

Nam, Fukuzumi, and coworkers have shown that the spectroscopic properties and chemical reactivity of $[Mn^{IV}(O)(N4py)]^{2+}$ are greatly perturbed by the addition of triflic acid (HOTf).[12] Upon the addition of acid, the 950 nm electronic absorption feature of $[Mn^{IV}(O)(N4py)]^{2+}$ decays and a shoulder at 550 nm is observed. An analysis of XAS data for $[Mn^{IV}(O)(N4py)]^{2+}$ in the presence of HOTf shows a dramatic drop in pre-edge intensity and an elongation in the Mn-oxo distance to 1.74 Å. These spectroscopic changes were attributed to the binding of two HOTf molecules to the Mn^{IV}-oxo unit of $[Mn^{IV}(O)(N4py)]^{2+}$.[12] Given that the proposed structure for this species is similar in spirit to that of $[Mn^{IV}(O)(N4py)]^{2+}\cdot(TFE)_2$, where two TFE molecules are bound to the Mn^{IV}-oxo unit through hydrogen-bonding interactions, we used DFT computations to investigate hypothetical structures for $[Mn^{IV}(O)(N4py)]^{2+}\cdot(HOTf)_2$.

The optimization of models of $[Mn^{IV}(O)(N4py)]^{2+}$ with triflic acid that included a CPCM for solvation invariably led to proton transfer between one of the second-sphere triflic acid

moieties and the oxo ligand (*vide infra*). This observation is accordant with the high acidity of triflic acid.[37] Only for optimizations performed in the gas-phase (*i.e.*, lacking a CPCM of solvation) did the triflic acid moieties retain their acidic protons. This change between CPCM and gas-phase calculations presumably derives from the lack of stabilization of charge separation in the gas phase. From the gas-phase optimizations, we identified minima for models of both $[Mn^{IV}(O)(N4py)]^{2+}\cdot(HOTf)_2$ and $[Mn^{IV}(O)(N4py)]^{2+}\cdot(HOTf)$, which contain two and one second-sphere triflic acid molecules, respectively (Figure S4). The Mn=O distances in the $[Mn^{IV}(O)(N4py)]^{2+}$–$(HOTf)_2$ and $[Mn^{IV}(O)(N4py)]^{2+}\cdot(HOTf)$ structures are 1.702 and 1.687 Å (Table S7). These values are only slightly longer than that predicted for $[Mn^{IV}(O)(N4py)]^{2+}$ in the absence of any hydrogen-bonding interactions (1.681 Å; see Table 4), and are significantly shorter than that determined for an EXAFS analysis of $[Mn^{IV}(O)(N4py)]^{2+}$ in the presence of triflic acid (1.74 Å).[12]

When CPCM was included to incorporate the effects of TFE solvation, the initial structure of $[Mn^{IV}(O)(N4py)]^{2+}\cdot(HOTf)$ underwent proton transfer from triflic acid to the Mn^{IV}-oxo unit during the geometry optimization procedure. We therefore refer to this model as $[Mn^{IV}(OH)(N4py)]^{3+}\cdot(OTf^{-})$ to represent the observed protonation states in the energy-minimized structure. (All attempts at developing models of $[Mn^{IV}(O)(N4py)]^{2+}\cdot(HOTf)_2$ using CPCM for TFE solvation resulted in optimized structures with large, negative frequencies; *i.e.*, these structures are not true minima). The structure of $[Mn^{IV}(OH)(N4py)]^{3+}\cdot(OTf^{-})$ has a Mn–OH distance of 1.757 Å, with the hydroxo ligand involved in a strong hydrogen-bonding interaction with the second-sphere triflate anion (Figure 6). The Mn–N distances show a very modest contraction relative to those of $[Mn^{IV}(O)(N4py)]^{2+}$ (Table 4 and Table S7). The DFT-predicted Mn–OH distance for $[Mn^{IV}(OH)(N4py)]^{3+}\cdot(OTf^{-})$ is slightly longer than that observed for $[Mn^{IV}(O)(N4py)]^{2+}$ in the presence of triflic acid (1.74 Å).[21] We also explored structures of $[Mn^{IV}(OH)(N4py)]^{3+}$ where the hydroxo ligand was involved in hydrogen-bonding interactions with second-sphere TFE solvent molecules. Although multiple starting structures were examined, the only system for which a true minimum was obtained involved a second-sphere TFE molecule and lacked a solvation model. In this structure, referred to as $[Mn^{IV}(OH)(N4py)]^{3+}\cdot(TFE)$, the Mn–OH distance is 1.749 Å, and the hydroxo ligand donates a hydrogen bond to one TFE molecule, resulting in a short hydroxo---H distance of 1.649 Å (Figure 6). A DFT structure of $[Mn^{IV}(OH)(N4py)]^{3+}$ in the absence of any second-sphere hydrogen-bonding interactions showed a longer Mn–OH distance of 1.773 Å (Figure 6 and Table S7), revealing that the Mn-oxygen bond length contracts when the hydroxo serves as a hydrogen-bond donor.

As a further means of assessing the validity of the Mn^{IV}-hydroxo models, we performed TD-DFT computations to predict electronic absorption spectra for $[Mn^{IV}(OH)(N4py)]^{3+}$, $[Mn^{IV}(OH)(N4py)]^{3+}\cdot(OTf^{-})$, and $[Mn^{IV}(OH)(N4py)]^{3+}\cdot(TFE)$. Our previously reported TD-DFT computations for $[Mn^{IV}(O)(N4py)]^{2+}$ predicted electronic absorption bands near 790 and 475 nm, with more intense features at wavelengths below 400 nm.[26] These results were in reasonable agreement with the experimental electronic absorption spectrum of $[Mn^{IV}(O)(N4py)]^{2+}$, which contains a prominent features near 950 nm, a weak band at ca. 600 nm, and intense features below 400 nm.[26, 38] The TD-DFT method predicts the electronic transitions to be too high in energy, and the computed band intensities were also ca. 3-fold higher than those observed experimentally.[26] The TD-DFT computed electronic

absorption spectra for $[Mn^{IV}(OH)(N4py)]^{3+}$, $[Mn^{IV}(OH)(N4py)]^{+}\cdot(OTf^{-})$, and $[Mn^{IV}(OH)(N4py)]^{3+}\cdot(TFE)$ each show prominent features at 425, 440, and 473 nm, respectively (Figure 7). The spectra no longer contain the 950 nm near-IR feature characteristic of $[Mn^{IV}(O)(N4py)]^{2+}$. These spectral changes are consistent with those observed by Nam, Fukuzumi, and coworkers upon the addition of triflic acid to $[Mn^{IV}(O)(N4py)]^{2+}$.[12] In that case, the 950 nm electronic absorption band of $[Mn^{IV}(O)(N4py)]^{2+}$ disappeared, and a new band at 550 nm gained intensity.[12] While the experimental band is lower in energy than that predicted for $[Mn^{IV}(OH)(N4py)]^{+}$, $[Mn^{IV}(OH)(N4py)]^{3+}\cdot(OTf^{-})$, or $[Mn^{IV}(OH)(N4py)]^{3+}\cdot(TFE)$ (Figure 7), this discrepancy is attributed to errors in the TD-DFT treatment. In support, an electronic absorption spectrum for $[Mn^{IV}(OH)(N4py)]^{2+}$ by CASSCF/NEVPT2 calculations shows Mn^{IV} ligand-field transitions at 529 and 434 nm (Figure 6, bottom). We previously showed that the CASSCF/NEVPT2 calculations for $[Mn^{IV}(O)(N4py)]^{2+}$ yields electronic transition energies in better agreement with experiment than the TD-DFT method.[26] Overall, the Mn^{IV}-hydroxo models, especially those where the hydroxo ligand is involved in hydrogen-bonding interactions, are consistent with the spectroscopic data collected when $[Mn^{IV}(O)(N4py)]^{2+}$ is treated with triflic acid. (We attempted to perform CASSCF/NEVPT2 calculations for the $[Mn^{IV}(OH)(N4py)]^{3+}\cdot(OTf^{-})$ and $[Mn^{IV}(OH)(N4py)]^{3+}\cdot(TFE)$ models, but these calculations were plagued by convergence issues. In addition, TD-DFT calculations for the gas-phase models of $[Mn^{IV}(O)(N4py)]^{2+}\cdot(HOTf)_2$ and $[Mn^{IV}(O)(N4py)]^{2+}\cdot(HOTf)$ were dominated by intense, and unphysical, charge-transfer transitions between the triflic acid moieties and the Mn^{IV} center.)

Discussion

Manganese(IV)-oxo adducts are important intermediates in both biological and synthetic oxidation reactions.[39] The development of structure-function relationships for these compounds are hindered by a paucity of experimental studies on the structural properties of manganese(IV)-oxo species. To the best of our knowledge, only a single mononuclear Mn^{IV}-oxo complex has been structurally characterized by XRD.[6] For the remainder of known Mn^{IV}-oxo complexes, Mn K-edge XAS has served as the sole technique for determining Mn-ligand bond distances. Herein, we utilized Mn K-edge XAS to determine metric parameters for a set of three Mn^{IV}-oxo species supported by N4py derivatives. Previous work had shown that these particular complexes display a range of rates for HAT and oxygen-atom transfer reactions, making the structures of these complexes of particular interest.[7b, 9–10]

Analysis of the EXAFS data for $[Mn^{IV}(O)(^{DMM}N4py)]^{2+}$ and $[Mn^{IV}(O)(2pyN2B)]^{2+}$ revealed Mn=O distances of 1.72 and 1.70 Å, respectively (Table 2). These distances are in excellent agreement with those of other Mn^{IV}-oxo species in a pseudo-octahedral geometry (Table 6). Specifically, $[Mn^{IV}(O)(N4py)]^{2+}$ and $[Mn^{IV}(O)(Bn\text{-}TPEN)]^{2+}$, which also feature neutral N5 ligands, both show comparable Mn=O distances of 1.69 Å.[7c, 10a] Mononuclear Mn^{IV}-oxo complexes supported by porphyrin ligands, or with *cis* hydroxo ligands, also display similar distances (1.69 and 1.71 Å, respectively).[6–7, 10a, b, 40] The Mn=O distance for $[Mn^{IV}(O)(2pyN2Q)]^{2+}$ determined by analysis of EXAFS data (1.76 Å) is a clear outlier among this set of complexes. We attribute this long distance to sample heterogeneity, which

is reasonable given that $[Mn^{IV}(O)(2pyN2Q)]^{2+}$ shows greatly reduced stability compared to the other Mn^{IV}-oxo complexes in this series.[9a] Thus, we do not attribute the 1.76 Å distance to the Mn=O bond length. (We note that, while it would be illuminating to compare $Mn–N_{axial}$ and average $Mn–N_{equatorial}$ distances for this series of Mn^{IV}-oxo complexes, it is not possible to attribute particular Mn–N EXAFS shells to these ligand types.)

Potential Role of Trifluoroethanol in Stabilizing Mn^{IV}-oxo Species.

While the Mn=O distances for $[Mn^{IV}(O)(^{DMM}N4py)]^{2+}$ and $[Mn^{IV}(O)(2pyN2B)]^{2+}$ determined from an analysis of EXAFS data agree well with other examples in the literature, these distances are in relatively poor to these ligand types.) agreement with the Mn=O distances from DFT calculations (Table 3). The computationally determined Mn=O distances for $[Mn^{IV}(O)(^{DMM}N4py)]^{2+}$ and $[Mn^{IV}(O)(2pyN2B)]^{2+}$ are each 0.04 Å lower than those determined from EXAFS analysis. Better agreement is achieved for calculations that included second-sphere TFE molecules, which form strong hydrogen-bonds with the oxo ligands (Figure 4). The hydrogen-bonds result in a slight elongation of the Mn=O distances, putting the computationally determined Mn=O distances for $[Mn^{IV}(O)(^{DMM}N4py)]^{2+}$ and $[Mn^{IV}(O)(2pyN2B)]^{2+}$ within 0.02 Å of those determined from the analysis of EXAFS data.

The intimate interactions between the Mn^{IV}-oxo unit and solvent predicted by these computations could offer insight into the privileged role that TFE has played in stabilizing Mn^{IV}-oxo species with neutral, N5 supporting ligands. Nam and co-workers were the first to observe that certain Mn^{IV}-oxo centers could form in excellent yield in TFE but not in other solvents.[7b, c] Although some of these Mn^{IV}-oxo adducts can be formed in mixed solvents, these mixtures always include TFE, *i.e.*, TFE:CH_2Cl_2 or TFE:MeCN. We have used this knowledge to great advantage to make our present series of Mn^{IV}-oxo complexes.[9a] While we have previously suggested a role for TFE in helping to solubilize PhIO,[9a] allowing for a rapid reaction with the Mn^{II} precursor complex, our present computations suggest that hydrogen-bonding with TFE serves to stabilize the Mn^{IV}-oxo unit. One test of this proposed role of TFE as a hydrogen-bond donor would be to measure EXAFS data for one of these Mn^{IV}-oxo complexes in an aprotic solvent. Unfortunately, formation of members of this class of Mn^{IV}-oxo species in an aprotic solvent has not yet been achieved.

Hydrogen-bonding Comparison for Mn^{IV}-oxo and Fe^{IV}-oxo species in TFE.

While the Mn^{IV}-oxo species supported by N4py derivatives and Bn-TPEN require the use of TFE as a solvent for formation, the analogous Fe complexes can be formed in either protic TFE or aprotic MeCN.[7b, c, 8a, 10a, 41] Thus, TFE is not the privileged solvent for Fe^{IV}-oxo complexes as it is for Mn^{IV}-oxo analogues. Our DFT computations for $[Fe^{IV}(O)(N4py)]^{2+}$ in the presence of two second-sphere TFE molecules show reduced solvent-oxo hydrogen-bonding interactions when compared to the Mn^{IV}-oxo counterpart. Specifically, the DFT-optimized structures for $[Fe^{IV}(O)(N4py)]^{2+}\cdot(TFE)_2$ shows oxo···H separations that are 0.1 Å longer than those for $[Mn^{IV}(O)(N4py)]^{2+}\cdot(TFE)_2$. Thus, solvent stabilization might not be as critical for the Fe^{IV}-oxo species.

This difference in hydrogen-bonding interactions is also relevant to reports that Mn^{IV}- and Fe^{IV}-oxo species exhibit different sensitivity to acids at parity of coordination sphere.[36] Both observations suggest that the basicity of the metal-oxo ligand is very different. The $[Mn^{IV}(O)(OH)(^{H,Me}Pytacn)]^{+}$ complex of Costas and co-workers can be readily protonated to form $[Mn^{IV}(OH)_2(^{H,Me}Pytacn)]^{+}$, and titrations reveal a pK_a for this Mn^{IV}-dihydroxo species of 7.1.[36a] In contrast, $[Fe^{IV}(O)(OH)(^{H,Me}Pytacn)]^{+}$ remains unprotonated even at a very acidic pH of 1.[36b] These observations indicate that, at parity of coordination sphere, the Mn^{IV}-oxo adduct is several pK_a units more basic than the Fe^{IV}-oxo adduct.[36b]

Other Fe^{IV}-oxo complexes supported by N4 and N5 ligands have been shown to be stable in the presence of excess acid, which provides further evidence for the low basicity of such complexes. Specifically, the addition of either 10 mM $HClO_4$ or 5 M CF_3COOH to $[Fe^{IV}(O)(N4py)]^{2+}$ results in minimal changes to the electronic absorption spectrum, indicating that the Fe^{IV}-oxo adduct is not protonated under these conditions.[42] This behavior is in stark contrast to the analogous Mn^{IV}-oxo species, $[Mn^{IV}(O)(N4py)]^{2+}$, which exhibits spectral changes upon the addition of HOTf.[12] Of the limited examples of Fe^{IV}-oxo species that do show reaction with acid, the site for protonation has been unexpected. When acid is added to $[Fe^{IV}(O)(H_3buea)]^{-}$, protonation was proposed to occur at the tripodal ligand rather than the oxo ligand.[43] The locus of ligand protonation in this case was strongly supported by spectroscopic data.[43]

DFT Investigation of $[Mn^{IV}(O)(N4py)]^{2+}\cdot(HOTf)_2$ Species.

Similar to our proposal of $[Mn^{IV}(O)(N4py)]^{2+}\cdot(TFE)_2$, the formation of $[Mn^{IV}(O)(N4py)]^{2+}\cdot(HOTf)_2$ was proposed when HOTf is added to $[Mn^{IV}(O)(N4py)]^{2+}$.[12] EXAFS analysis showed a 0.04 Å elongation of the Mn=O distance upon addition of acid to $[Mn^{IV}(O)(N4py)]^{2+}$. Our gas-phase calculations for $[Mn^{IV}(O)(N4py)]^{2+}$ in the presence of second-sphere triflic acid molecules show little change in the Mn=O distance, suggesting that the 1.74 Å bond length is too long for a Mn^{IV}-oxo species with only hydrogen-bonding interactions. Importantly, calculations performed using a CPCM for solvation invariably showed proton transfer from triflic acid to the oxo ligand. These formal Mn^{IV}-hydroxo models showed metric and spectroscopic parameters reasonably consistent with the available data for $[Mn^{IV}(O)(N4py)]^{2+}$ in the presence of triflic acid (Figures 6 and 7).

The experimental spectral changes observed for $[Mn^{IV}(O)(N4py)]^{2+}$ upon the addition of acid consist of a loss of a near-IR absorption feature at 950 nm and the growth of a shoulder near 550 nm. These spectral changes are not only reasonably reproduced from our TD-DFT and CASCF/NEVPT2 calculations performed for models of $[Mn^{IV}(OH)(N4py)]^{2+}$ (Figure 7), the changes are also similar to those observed for pairs of Mn^{IV}-oxo and Mn^{IV}-hydroxo complexes. The $[Mn^{IV}(O)(OH)(Me_2EBC)]^{2+}$ complex and its protonated analogue $[Mn^{IV}(OH)_2(Me_2EBC)]^{2+}$ display electronic absorption maxima at 870 and 550 nm, respectively.[44] Likewise, the $[Mn^{IV}(O)(OH)(^{H,Me}Pytacn)]^{+}$ and $[Mn^{IV}(OH)_2(^{H,Me}Pytacn)]^{2+}$ complexes have electronic absorption bands near 810 and 540 nm, respectively.[36a] These changes in electronic transition energies were described in terms of the reduction in the Mn=O bond order, and the accompanied elimination of strong Mn-oxo π-interactions, upon protonation of the oxo ligand.[44] Specifically, the near-IR

absorption feature for these pseudo-octahedral Mn^{IV}-oxo complexes arises from a one-electron excitation from the Mn^{IV} d_{xz}, d_{yz} molecular orbitals (MOs), which are Mn=O π-antibonding, to the Mn^{IV} $d_{x^2-y^2}$ MO, which is Mn–$N_{equatorial}$ σ-antibonding. A shift of this near-IR absorption band to higher energy is consistent with a stabilization of the Mn^{IV} d_{xz}, d_{yz} donor orbitals through a weakening of Mn=O π-interactions. Thus, the similar spectral changes observed for $[Mn^{IV}(O)(OH)(Me_2EBC)]^{2+}$ and $[Mn^{IV}(O)(N4py)]^{2+}$ upon the addition of acid could suggest the formation of Mn^{IV}-hydroxo products for both systems.[44]

Conclusions

Analysis of Mn K-edge XAS data for $[Mn^{IV}(O)(2pyN2B)]^{2+}$ and the related $[Mn^{IV}(O)(^{DMM}N4py)]^{2+}$ and $[Mn^{IV}(O)(2pyN2Q)]^{2+}$ complexes yield large pre-edge areas and relatively short Mn=0 distances, which are hallmarks of mononuclear Mn^{IV}-oxo centers. Variations in pre-edge area are observed for this series, and these are well-reproduced by TD-DFT computations. The EXAFS-determined Mn=O bond lengths for these complexes are best reproduced by DFT models including second-sphere TFE molecules involved in strong hydrogen-bonding interactions with the oxo ligands. These interactions could shed light on the privileged status of TFE in stabilizing Mn^{IV}-oxo complexes. Weaker solvent-oxo hydrogen-bonding interactions were predicted for the Fe^{IV}-oxo complex $[Fe^{IV}(O)(N4py)]^{2+}$. This result is consistent with previous studies that suggest the Mn^{IV}-oxo unit is more basic than its Fe^{IV}-oxo counterpart. DFT investigations to understand the structure of $[Mn^{IV}(O)(N4py)]^{2+}$ in the presence of triflic acid led to the postulate that the trific acid protonates the Mn^{IV}-oxo unit to generate a Mn^{IV}-hydroxo center.

Supplementary Material

Refer to Web version on PubMed Central for supplementary material.

Acknowledgements.

This work was supported by the U.S. D.O.E. (DE-SC0016359). A.S. thanks the Carl Trygger Foundation for a postdoctoral fellowship. M.C.D. was supported by the NIH Graduate Traineeship T32 GM08545. The U.S. N.S.F. is acknowledged for funds used to support the purchase of EPR and X-ray instrumentation (CHE-0946883 and CHE-0923449). Use of the Stanford Synchrotron Radiation Lightsource, SLAC National Accelerator Laboratory, is supported by the U.S. Department of Energy, Office of Science, Office of Basic Energy Sciences under Contract No. DE-AC02-76SF00515. The SSRL Structural Molecular Biology Program is supported by the DOE Office of Biological and Environmental Research, and by the National Institutes of Health, National Institute of General Medical Sciences (including P41GM103393). The contents of this publication are solely the responsibility of the authors and do not necessarily represent the official views of NIGMS or NIH.

References

[1]. a)Rittle J and Green MT, Science 2010, 330, 933–937; [PubMed: 21071661] b)Huang X and Groves JT, Chem. Rev. 2017;c)Wong SD, Srnec M, Matthews ML, Liu LV, Kwak Y, Park K, Bell Iii CB, Alp EE, Zhao J, Yoda Y, Kitao S, Seto M, Krebs C, Bollinger JM and Solomon EI, Nature 2013, 499, 320; [PubMed: 23868262] d)Srnec M, Wong SD, Matthews ML, Krebs C, Bollinger JM and Solomon EI, J. Am. Chem. Soc 2016, 138, 5110–5122; [PubMed: 27021969] e)Price JC, Barr EW, Glass TE, Krebs C and Bollinger JM, J. Am. Chem. Soc 2003, 125, 13008–13009. [PubMed: 14570457]

[2]. Denisov IG, Makris TM, Sligar SG and Schlichting I, Chem. Rev. 2005, 105, 2253–2278. [PubMed: 15941214]

[3]. Hausinger RP, Critical Reviews in Biochemistry and Molecular Biology 2004, 39, 21–68. [PubMed: 15121720]

[4]. a)Puri M and Que L, Acc. Chem. Res 2015, 48, 2443–2452; [PubMed: 26176555] b)Nam W, Acc. Chem. Res 2015, 48, 2415–2423. [PubMed: 26203519]

[5]. Rohde J-U, In J-H, Lim MH, Brennessel WW, Bukowski MR, Stubna A, Munck E, Nam W and Que L, Science 2003, 299, 1037–1039. [PubMed: 12586936]

[6]. Halbach RL, Gygi D, Bloch ED, Anderson BL and Nocera DG, Chem. Sci 2018, 9, 4524–4528. [PubMed: 29896395]

[7]. a)Leto DF, Massie AA, Colmer HE and Jackson TA, Inorg. Chem. 2016, 55, 3272–3282; [PubMed: 27002928] b)Chen J, Lee Y-M, Davis KM, Wu X, Seo MS, Cho K-B, Yoon H, Park YJ, Fukuzumi S, Pushkar YN and Nam W, J. Am. Chem. Soc 2013, 135, 6388–6391; [PubMed: 23324100] c)Wu X, Seo MS, Davis KM, Lee Y-M, Chen J, Cho K-B, Pushkar YN and Nam W, J. Am. Chem. Soc 2011, 133, 20088–20091. [PubMed: 22091637]

[8]. a)Chen J, Cho K-B, Lee Y-M, Kwon YH and Nam W, Chem. Commun 2015, 51, 13094–13097;b)Cho K-B, Shaik S and Nam W, The Journal of Physical Chemistry Letters 2012, 3, 2851–2856.

[9]. a)Massie AA, Denler MC, Cardoso LT, Walker AN, Hossain MK, Day VW, Nordlander E and Jackson TA, Angew. Chem. Int. Ed 2017, 56, 4178–4182;b)Denler MC, Massie AA, Singh R, Stewart-Jones E, Sinha A, Day VW, Nordlander E and Jackson TA, Dalton Trans. 2019, 48, 5007–5021. [PubMed: 30916103]

[10]. a)Leto DF, Ingram R, Day VW and Jackson TA, Chem. Commun 2013, 49, 5378–5380;b)Kurahashi T, Kikuchi A, Tosha T, Shiro Y, Kitagawa T and Fujii H, Inorg. Chem 2008, 47, 1674–1686; [PubMed: 18237118] c)Leto DF and Jackson TA, Inorg. Chem 2014, 53, 6179–6194. [PubMed: 24901026]

[11]. Penner-Hahn JE in X-ray Absorption Spectroscopy, Vol. 2 Elsevier Ltd, 2003, pp. 159–186.

[12]. Chen J, Yoon H, Lee Y-M, Seo MS, Sarangi R, Fukuzumi S and Nam W, Chem. Sci 2015, 6, 3624–3632. [PubMed: 26146538]

[13]. Wijeratne GB, Corzine B, Day VW and Jackson TA, Inorg. Chem 2014, 53, 7622–7634. [PubMed: 25010596]

[14]. Seo MS, Kim JY, Annaraj J, Kim Y, Lee Y-M, Kim S-J, Kim J and Nam W, Angew. Chem. Int. Ed 2007, 46, 377–380.

[15]. Saltzman H and Sharefkin JG, Org. Synth 1963, 43, 60.

[16]. Mitra M, Nimir H, Demeshko S, Bhat SS, Malinkin SO, Haukka M, Lloret-Fillol J, Lisensky GC, Meyer F, Shteinman AA, Browne WR, Hrovat DA, Richmond MG, Costas M and Nordlander E, Inorg. Chem 2015, 54, 7152–7164. [PubMed: 26198840]

[17]. Ravel B and Newville M, J. Synchrotron Rad 2005, 12, 537–541.

[18]. Rehr JJ, Mustre de Leon J, Zabinsky SI and Albers RC, J. Am. Chem. Soc 1991, 113, 5135–5140.

[19]. Penner-Hahn JE, Coord. Chem. Rev 1999, 190–192, 1101–1123.

[20]. Wojdyr M, J. Appl. Crystallogr 2010, 43, 1126–1128.

[21]. Neese F, Wiley Interdisciplinary Reviews: Computational Molecular Science 2012, 2, 73–78.

[22]. Tao J, Perdew JP, Staroverov VN and Scuseria GE, Phys. Rev. Lett 2003, 91, 146401. [PubMed: 14611541]

[23]. a)Grimme S, Antony J, Ehrlich S and Krieg H, J. Chem. Phys 2010, 132, 154104; [PubMed: 20423165] b)Grimme S, Ehrlich S and Goerigk L, Journal of Computational Chemistry 2011, 32, 1456–1465. [PubMed: 21370243]

[24]. a)Schafer A, Horn H and Ahlrichs R, J. Chem. Phys 1992, 97, 2571–2577;b)Schafer A, Huber C and Ahlrichs R, J. Chem. Phys 1994, 100, 5829–5835;c)Weigend F and Ahlrichs R, Phys. Chem. Chem. Phys 2005, 7, 3297–3305. [PubMed: 16240044]

[25]. Marenich AV, Cramer CJ and Truhlar DG, The Journal of Physical Chemistry B 2009, 113, 6378–6396. [PubMed: 19366259]

[26]. Leto DF, Massie AA, Rice DB and Jackson TA, J. Am. Chem. Soc 2016, 138, 15413–15424. [PubMed: 27802057]

[27]. Boese AD, ChemPhysChem 2015, 16, 978–985. [PubMed: 25688988]

[28]. Brink CP and Crumbliss AL, Inorg. Chem 1984, 23, 4708–4718.

[29]. Massie AA, Denler MC, Cardoso LT, Walker AN, Hossain MK, Day VW, Nordlander E and Jackson TA, Angew. Chem. Int. Ed 2017, 56, 4178–4182.

[30]. Neese F, JBIC Journal of Biological Inorganic Chemistry 2006, 11, 702–711. [PubMed: 16821037]

[31]. Rasheed W, Draksharapu A, Banerjee S, Young VG, Fan R, Guo Y, Ozerov M, Nehrkorn J, Krzystek J, Telser J and Que L, Angew. Chem. Int. Ed 2018, 57, 9387–9391.

[32]. Although little variation is seen in the transition energies between the MnIV-oxo models with or without the hydrogen-bonding TFE molecules, the models lacking the hydrogen-bonding interactions show slightly higher pre-edge intensities (increase of ca. 4 units; see Table S4). This increase in intensity is readily attributed to the shorter Mn(O distances for the models lacking the hydrogen-bonding interactions. Because of the minor variations between models with and without TFE molecules, we focus our discussion on the latter.

[33]. Leto DF and Jackson TA, Inorg. Chem 2014, 53, 6179–6194. [PubMed: 24901026]

[34]. Klinker EJ, Kaizer J, Brennessel WW, Woodrum NL, Cramer CJ and Que L Jr., Angew. Chem. Int. Ed 2005, 44, 3690–3694.

[35]. a)Decker A, Rohde J-U, Klinker EJ, Wong SD, Que L Jr. and Solomon EI, J. Am. Chem. Soc 2007, 129, 15983–15996; [PubMed: 18052249] b)Klinker EJ, Shaik S, Hirao H and Que L, Angew. Chem. Int. Ed 2009, 48, 1291–1295;c)Hirao H, Kumar D, Que L Jr. and Shaik S, J. Am. Chem. Soc 2006, 128, 8590–8606. [PubMed: 16802826]

[36]. a)Garcia-Bosch I, Company A, Cady CW, Styring S, Browne WR, Ribas X and Costas M, Angew. Chem., Int. Ed 2011, 50, 5648–5653;b)Company A, Prat I, Frisch JR, Mas-Ballesté DR, Güell M, Juhász G, Ribas X, Münck DE, Luis JM, Que L and Costas M, Chemistry - A European Journal 2011, 17, 1622–1634.

[37]. Trummal A, Lipping L, Kaljurand I, Koppel IA and Leito I, The Journal of Physical Chemistry A 2016, 120, 3663–3669. [PubMed: 27115918]

[38]. Leto DF, Ingram R, Day VW and Jackson TA, Chem. Commun 2013, 49, 5378–5380.

[39]. a)Ray K, Pfaff FF, Wang B and Nam W, J. Am. Chem. Soc 2014, 136, 13942–13958; [PubMed: 25215462] b)Neu HM, Baglia RA and Goldberg DP, Acc. Chem. Res 2015, 48, 2754–2764; [PubMed: 26352344] c)Guo M, Corona T, Ray K and Nam W, ACS Central Science 2019, 5, 13–28. [PubMed: 30693322]

[40]. Charnock JM, Gamer CD, Trautwein AX, Bill E, Winkler H, Ayougou K, Mandon D and Weiss R, Angew. Chem. Int. Ed 1995, 34, 343–346.

[41]. Kaizer J, Klinker EJ, Oh NY, Rohde J-U, Song WJ, Stubna A, Kim J, Miinck E, Nam W and Que L, J. Am. Chem. Soc 2004, 126, 472–473. [PubMed: 14719937]

[42]. a)Park J, Lee Y-M, Nam W and Fukuzumi S, J. Am. Chem. Soc 2013, 135, 5052–5061; [PubMed: 23528016] b)Wang D, Zhang M, Bühlmann P and Que L, J. Am. Chem. Soc 2010, 132, 7638–7644. [PubMed: 20476758]

[43]. Hill EA, Weitz AC, Onderko E, Romero-Rivera A, Guo Y, Swart M, Bominaar EL, Green MT, Hendrich MP, Lacy DC and Borovik AS, J. Am. Chem. Soc 2016,138, 13143–13146. [PubMed: 27647293]

[44]. Chattopadhyay S, Geiger RA, Yin G, Busch DH and Jackson TA, Inorg. Chem 2010, 49, 7530–7535. [PubMed: 20690762]

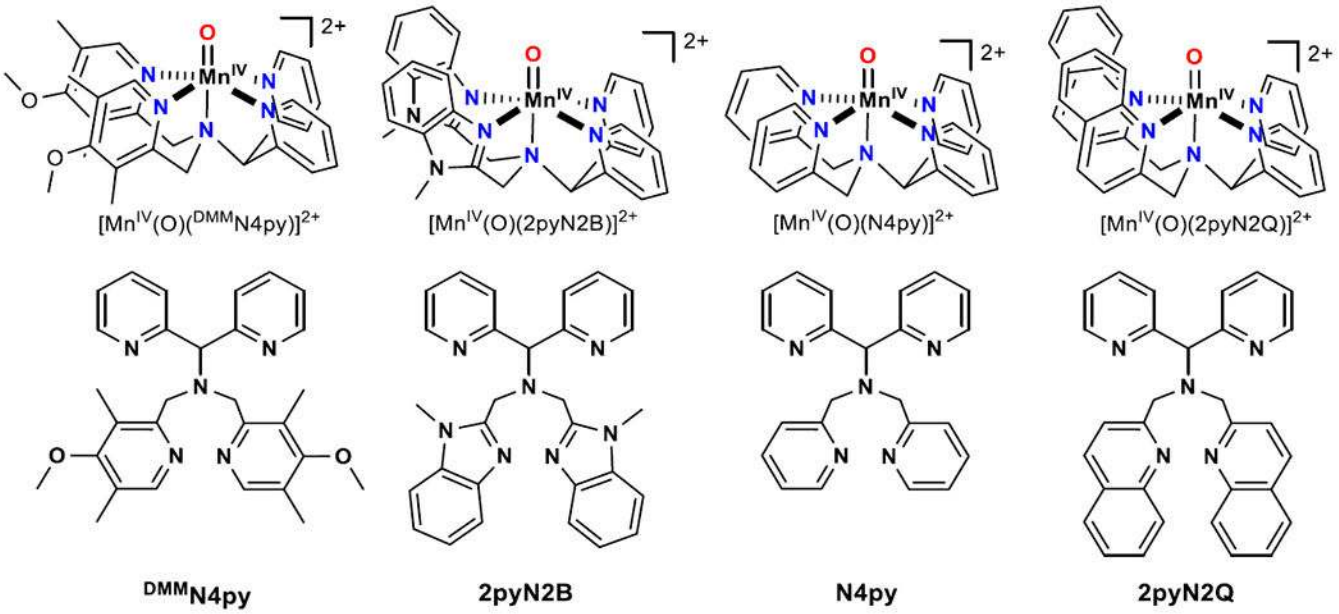

Figure 1.
Mn^{IV}-oxo complexes and their corresponding ligands based on N4py ligand framework.

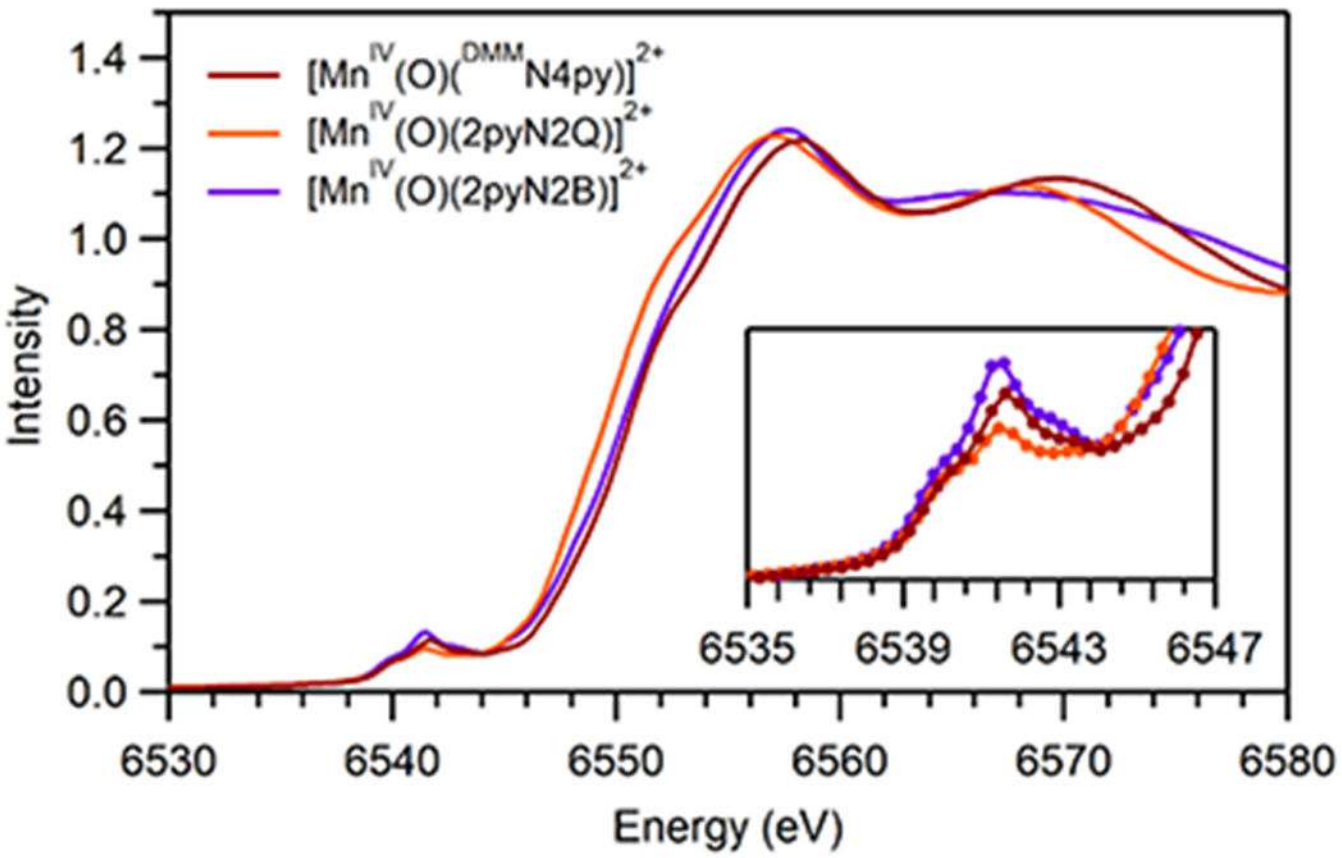

Figure 2.

Comparison of experimental XANES regions for $[Mn^{IV}(O)(^{DMM}N4py)]^{2+}$, $[Mn^{IV}(O)2pyN2B)]^{2+}$, and $[Mn^{IV}(O)(2pyN2Q)]^{2+}$. The inset shows the near-edge features as the collected data points (circles) to display the resolution in this spectral region.

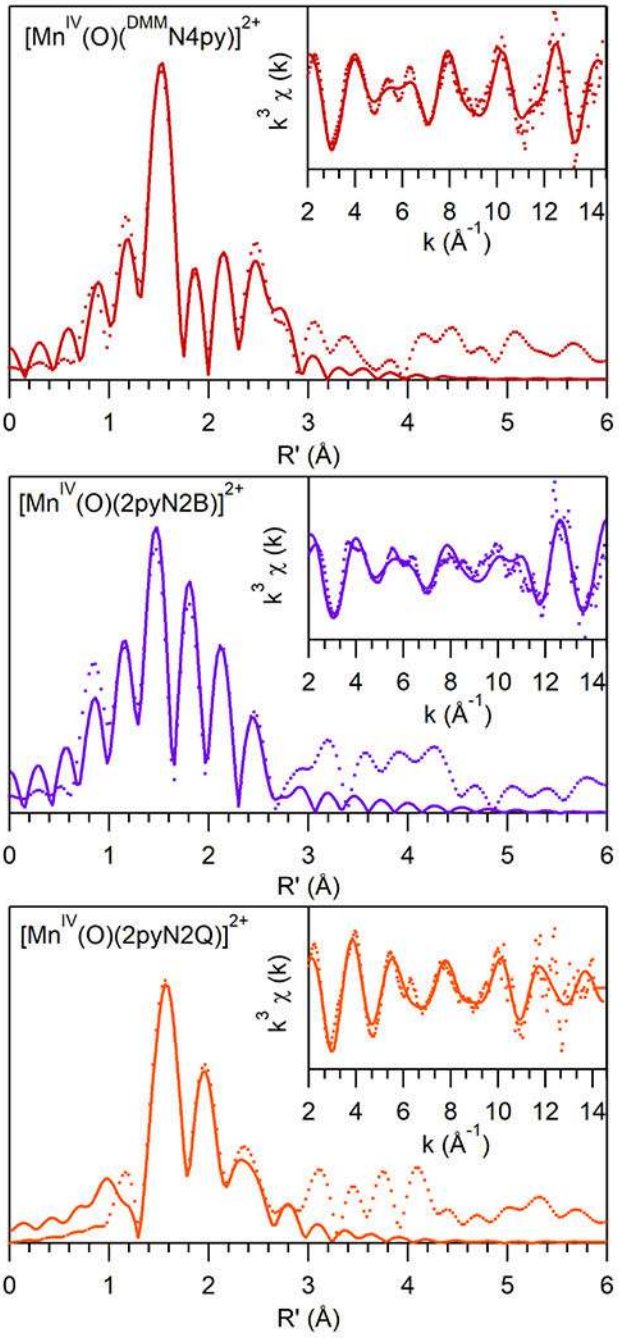

Figure 3.

Fourier transforms of Mn K-edge EXAFS data and raw k^3 weighted EXAFS curves (insets) for the Mn^{IV}-oxo species. Experimental data are represented by dotted lines whereas fits are solid lines.

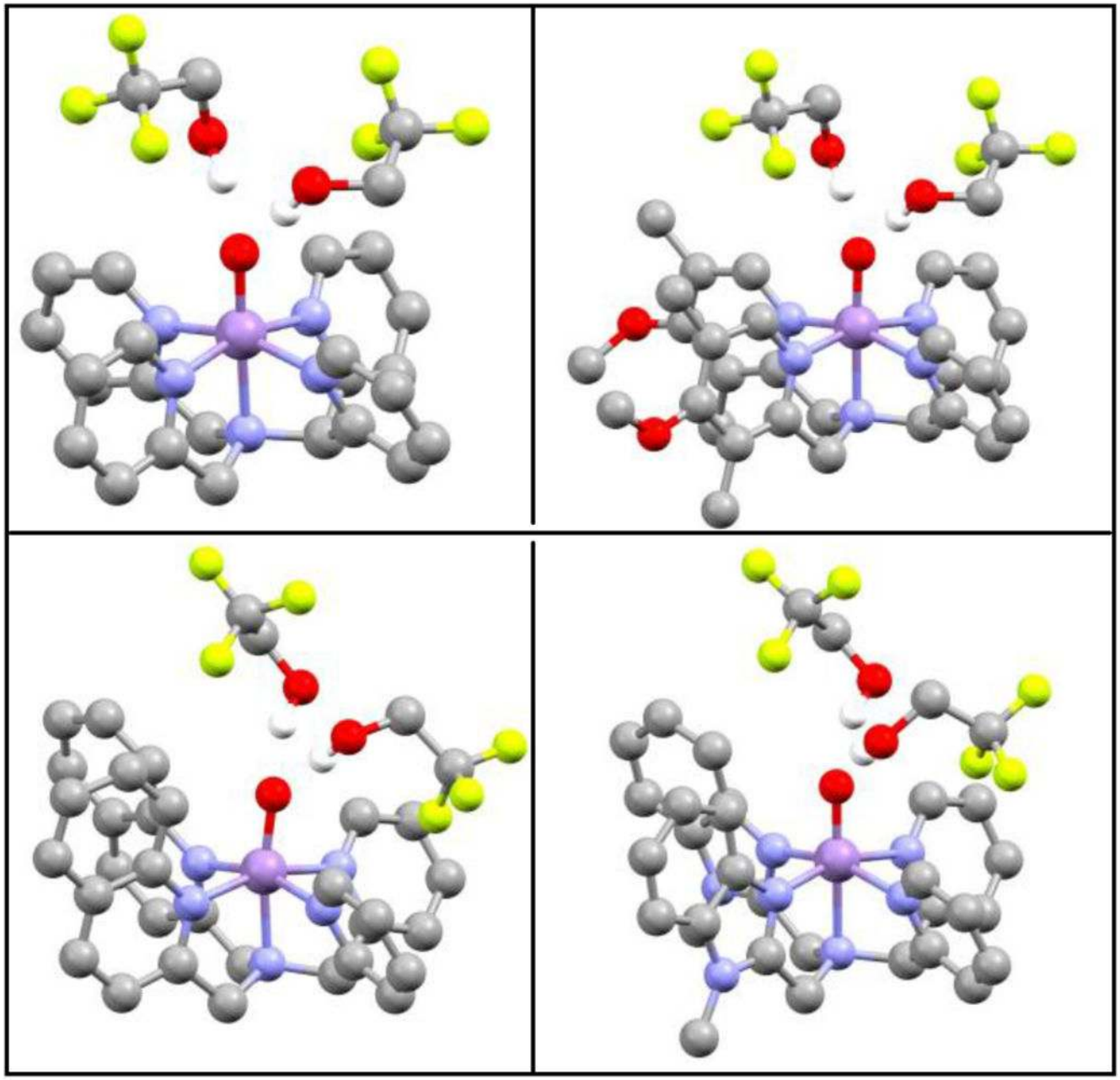

Figure 4.

Molecular structures of Mn^{IV}-oxo complexes, $[Mn^{IV}(O)(N4py)]^{2+}\cdot(TFE)_2$ (top-left), $[Mn^{IV}(O)(^{DMM}N4py)]^{2+}\cdot(TFE)_2$ (top-right), $[Mn^{IV}(O)(2pyN2Q)]^{2+}\cdot(TFE)_2$ (bottom-left), and $[Mn^{IV}(O)(2pyN2B)]^{2+}\cdot(TFE)_2$ (bottom-right). Alternate views of these structures are provided in the Supporting Information (Figure S3).

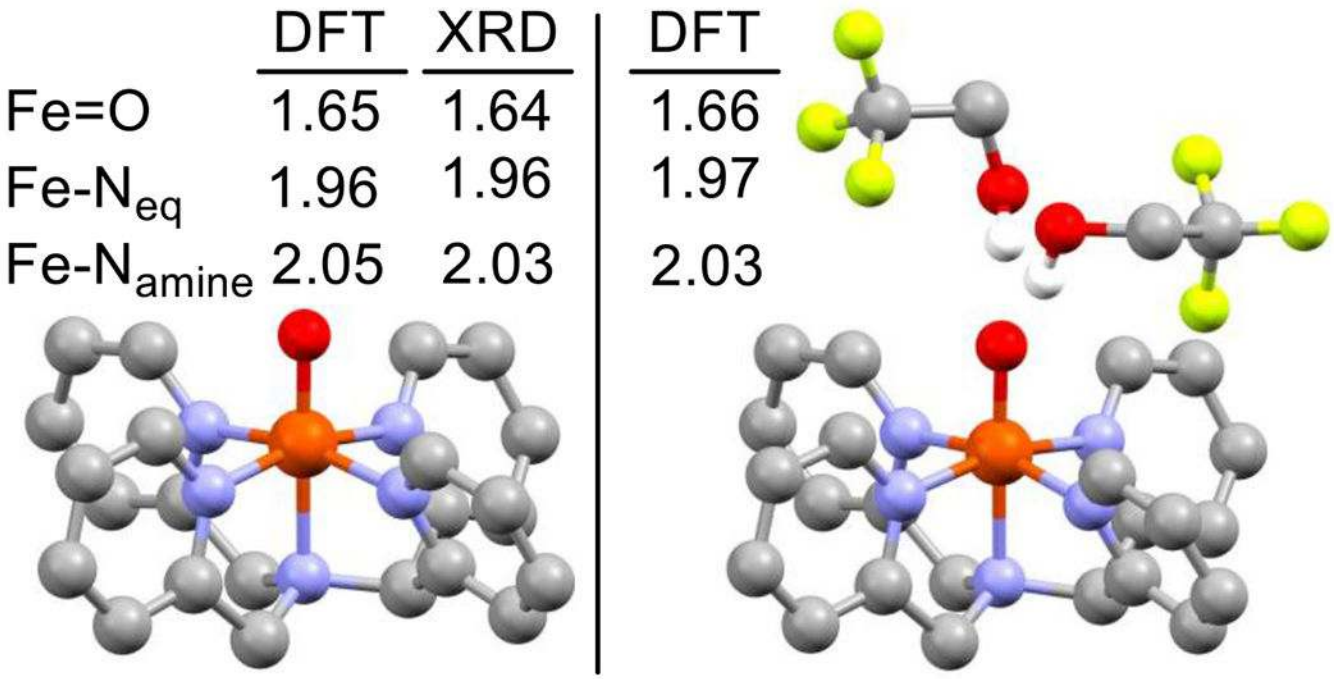

Figure 5.

Molecular structures of $[Fe^{IV}(O)(N4py)]^{2+}$ (left) and $[Fe^{IV}(O)(N4py)]^{2+}\cdot(TFE)_2$ (right). Metric parameters from DFT computations and the X-ray diffraction (XRD) structure of $[Fe^{IV}(O)(N4py)](OTf)_2$ are provided. XRD data are from reference [34].

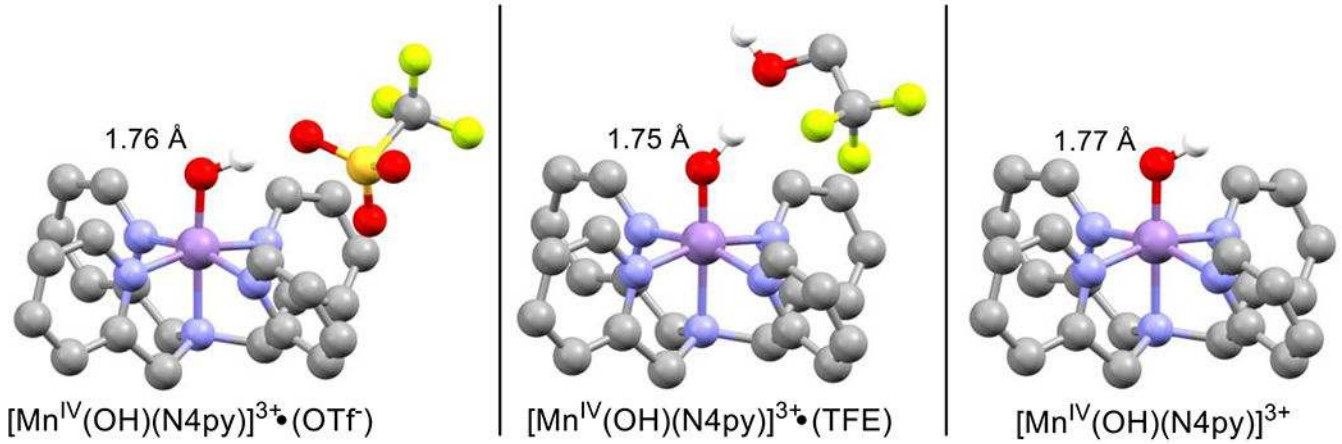

Figure 6.

Molecular structures of $[Mn^{IV}(OH)(N4py)]^{3+}\cdot(OTf)$ (left), $[Mn^{IV}(OH)(N4py)]^{3+}\cdot(TFE)$ (center), and $[Mn^{IV}(OH)(N4py)]^{3+}$ (right) from DFT geometry optimizations. The Mn–O distances are marked.

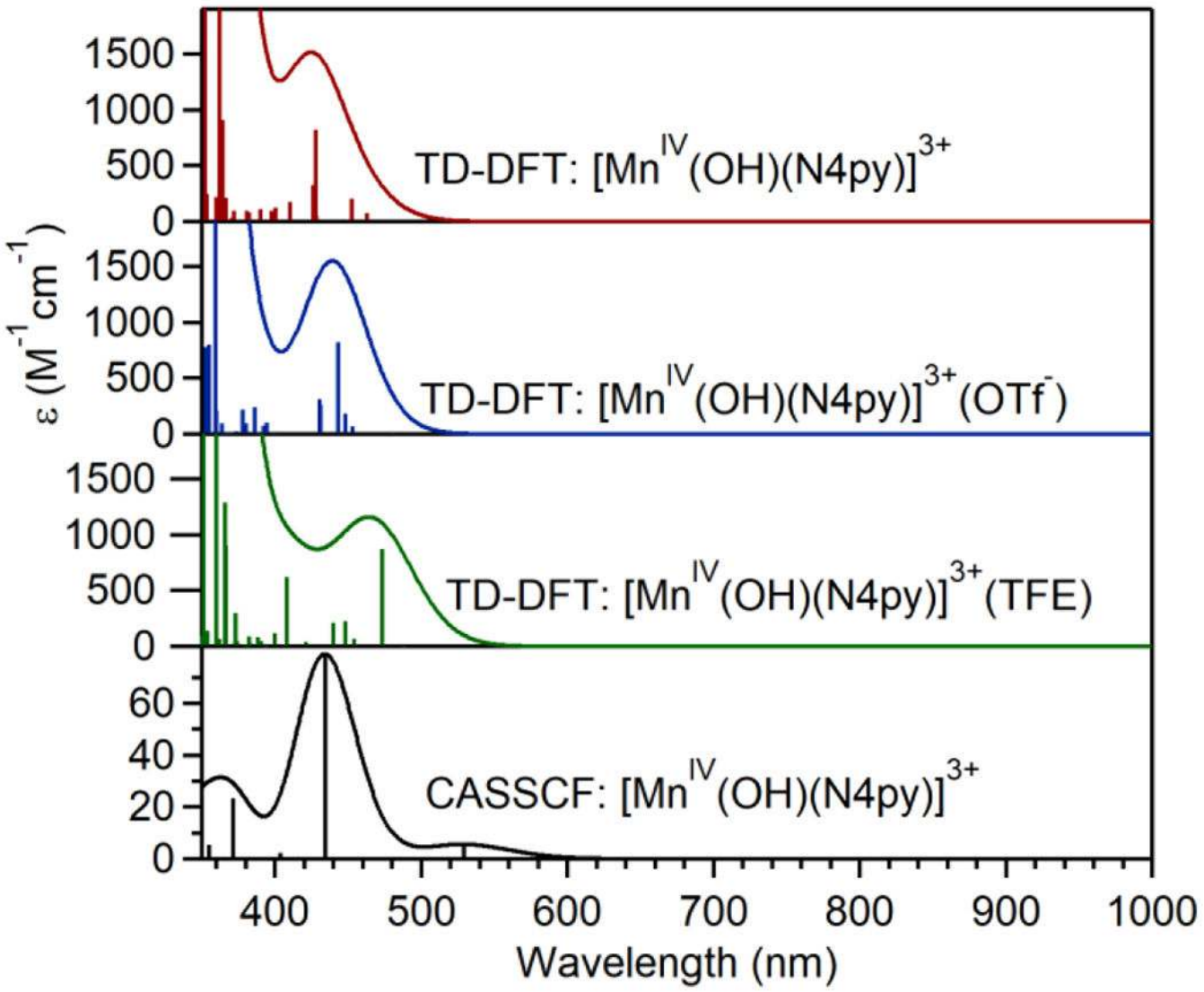

Figure 7.

Electronic absorption spectra for Mn^{IV}-hydroxo models using TD-DFT and CASSCF/NEVPT2 computations. Vertical sticks represent individual electronic transitions.

Table 1.

Edge and Pre-edge Energies (eV) and Pre-edge Areas for Mn^{IV}-oxo Complexes.

complex	edge energy	pre-edge energy	pre-edge area
$[Mn^{IV}(O)(^{DMM}N4py)]^{2+}$	6550.5 (6550.3)[b]	6539.9, 6541.6, 6543.2 (6541.2)[b]	20.1[a]
$[Mn^{IV}(O)(2pyN2B)]^{2+}$	6550.2 (6549.6)[b]	6539.9, 6541.4, 6542.8 (6540.1, 6541.4, 6543.1)[b]	22.2
$[Mn^{IV}(O)(N4py)]^{2+}$ [c]	6550.8	6541.9	18.9
$[Mn^{IV}(O)(2pyN2Q)]^{2+}$	6549.8 (6549.2)[b]	6539.9, 6541.5[d] (6541.2)[b]	15.1[a]

[a]Previously published data, using different samples, provided the following edge areas: 19.6 for $[Mn^{IV}(O)(^{DMM}N4py)]^{2+}$; 14.6 for $[Mn^{IV}(O)(2pyN2B)]^{2+}$; and 17.0 for $[Mn^{IV}(O)(2pyN2Q)]^{2+}$.

[b]Edge and pre-edge energies in parentheses from references [9a] and [9b].

[c]From reference [10a]. The previously reported pre-edge area for $[Mn^{IV}(O)(N4py)]^{2+}$ (12.7) used a normalization relative to the most intense fluorescence peak. This present value was obtained by normalizing the intensity to the tail of the EXAFS region.

[d]The pre-edge feature for $[Mn^{IV}(O)(2pyN2Q)]^{2+}$ can be fit with three pseudo-Voigt functions, but the fit is of similar quality to the two-band fit presented here.

Table 2.

Parameters derived from the best EXAFS fit for each Mn^{IV}-oxo complex

	Mn–O/N			Mn–N			Mn–C				
complex	***n***	**r(Å)**	**σ^2**	***n***	**r(Å)**	**σ^2**	***n***	**r(Å)**	**σ^2**	**E_0**	**R**
$[Mn^{IV}(O)(^{DMM}N4py)]^{2+}$	1	1.72	1.26	2	1.94	2.38	3	2.92	2.28	−1.79	0.208
				3	2.10	6.09	3	2.74	8.63		
$[Mn^{IV}(O)(2pyN2B)]^{2+}$	1	1.70	2.12	2	1.92	1.31	3	2.94	5.97	−4.01	0.304
				3	2.10	4.10	3	2.74	7.74		
$[Mn^{IV}(O)(2pyN2Q)]^{2+}$	1	1.76	7.06	3	2.06	6.31	4	2.91	7.34	−0.65	0.268
				2	2.25	5.73	3	2.71	8.17		

[a]Fourier Transform ranges are as follows: $[Mn^{IV}(O)(^{DMM}N4py)]^{2+}$: 2-14 $Å^{-1}$, $[Mn^{IV}(O)(2pyN2B)]^{2+}$: 2-13 $Å^{-1}$, $[Mn^{IV}(O)(2pyN2Q)]^{2+}$: 2-14 $Å^{-1}$.

[b]σ^2 is in units of 10^{-3} $Å^2$.

Table 3.

Comparison of DFT and EXAFS determined bond distances (Å) Mn^{IV}-oxo complexes.

complex	shell	DFT	EXAFS	DFT (H-bonding)
$[Mn^{IV}(O)(^{DMM}N4py)]^{2+}$	Mn–O (1)	1.68	1.72	1.70
	Mn–N (2)	1.99	1.95	1.98
	Mn–N (3)	2.04	2.10	2.03
$[Mn^{IV}(O)(2pyN2B)]^{2+}$	Mn–O (1)	1.66	1.70	1.68
	Mn–N (2)	1.97	1.92	1.96
	Mn–N (3)	2.20	2.10	2.08

Table 4.

Selected Bond Lengths (Å), Bond Angles (°), and Hydrogen-Bonding Distances (Å) for Mn^{IV}-oxo Complexes $[Mn^{IV}(O)(N4py)]^{2+}$, $[Mn^{IV}(O)(^{DMM}N4py)]^{2+}$, $[Mn^{IV}(O)(2pyN2B)]^{2+}$, and $[Mn^{IV}(O)(2pyN2Q)]^{2+}$ from DFT Computations.[a]

	Mn–O	Mn–N_{eq}[b]	Mn–N_{amine}[c]	O–Mn–N_{amine}	O···H[d]
$[Mn^{IV}(O)(N4py)]^{2+}$	1.681	2.001	2.097	179.65	NA[e]
$[Mn^{IV}(O)(N4py)]^{2+}\cdot(TFE)_2$	1.699	2.001	2.077	178.27	1.641, 1.651
$[Mn^{IV}(O)(^{DMM}N4py)]^{2+}$	1.682	1.998	2.089	179.28	NA[e]
$[Mn^{IV}(O)(^{DMM}N4py)]^{2+}\cdot(TFE)_2$	1.702	1.997	2.069	177.97	1.622, 1.653
$[Mn^{IV}(O)(2pyN2B)]^{2+}$	1.661	2.055	2.335	176.03	NA[e]
$[Mn^{IV}(O)(2pyN2B)]^{2+}\cdot(TFE)_2$	1.680	1.999	2.155	178.24	1.739, 1.749
$[Mn^{IV}(O)(2pyN2Q)]^{2+}$	1.684	2.032	2.088	170.14	NA[e]
$[Mn^{IV}(O)(2pyN2Q)]^{2+}\cdot(TFE)_2$	1.703	2.030	2.070	170.44	1.678, 1.703

[a] Additional metric parameters for these models are in supporting intormation (Table S6).

[b] The average of the four equatorial Mn–N bond lengths.

[c] N_{amine} refers to the amine nitrogen *trans* to the oxo ligand.

[d] Distances between the oxo ligand the alcohol hydrogen atoms of the TFE molecules.

[e] Not applicable.

Table 5.

Experimental and TD-DFT-Calculated Pre-edge Energies (eV) and Areas for the Series of Mn^{IV}-oxo Complexes.

	experimental		calculated pre-edge properties[a]			
complex	**pre-edge**	**area**	**pre-edge energy**	**intensity**	**area**	**Mn 4p**
$[Mn^{IV}(O)(^{DMM}N4py)]^{2+}$	6539.9	20.1	6541.0	2.58	17.3	3.1
	6541.6		6542.0			
	6543.2		6543.0			
$[Mn^{IV}(O)(2pyN2B)]^{2+}$	6539.9	22.2	6540.9	3.80	24.7	5.1
	6541.4		6541.9			
	6542.8		6542.9			
$[Mn^{IV}(O)(N4py)]^{2+}$	6541.9[b]	18.9[b]	6542.2	2.67	17.8	3.2
			6543.2			
$[Mn^{IV}(O)(2pyN2Q)]^{2}+$	6539.9	15.1	6541.6	2.34	15.9	2.0
	6541.5		6542.0			
			6542.9			

[a] From TD-DFT computations for models of the Mn^{IV}-oxo complexes with second-sphere TFE molecules hydrogen-bonding to the oxo ligand. Corresponding properties for models lacking the TFE molecules are included in the Supporting Information (Table S4).

[b] From references [10a] and [7b]

Table 6.

Selected Bond Lengths (Å) for Mononuclear Mn^{IV}-oxo Complexes from EXAFS and XRD Data.

Complex	Mn=O	Solvent	Reference
$[Mn^{IV}(O)(N4py)]^{2+}$	1.69, 1.70	TFE	[10a] [7b]
$[Mn^{IV}(O)(N4py)]^{2+}\cdot(HOTf)_2$	1.74	TFE/MeCN	[12]
$[Mn^{IV}(O)(^{DMM}N4py)]^{2+}$	1.72	TFE	*a*
$[Mn^{IV}(O)(2pyN2B)]^{2+}$	1.70	TFE	*a*
$[Mn^{IV}(O)(OH)(Me_2EBC)]^{+}$	1.71	H_2O	[7a]
$[Mn^{IV}(O)(Bn\text{-}TPEN)]^{2+}$	1.69	TFE	[7c]
$[Mn^{IV}(O)(T_{piv}PP)]$	1.69	THF/DMF	[40]
$[Mn^{IV}(O)(salen)]$	1.58	PrCN	[10b]
$[Mn^{IV}(O)(ditox)_3]^{-}$	1.63	*b*	[6]

*a*This work.

*b*Distance determined from solid-state XRD measurement.